2013

External Cavity Mode-locked Semiconductor Lasers For The Generation Of Ultra-low Noise Multi-gigahertz Frequency Combs And Applications In Multi-heterodyne Detection Of Arbitrary Optical Waveforms

Josue Davila-Rodriguez
University of Central Florida

EXTERNAL CAVITY MODE-LOCKED SEMICONDUCTOR LASERS FOR THE GENERATION OF ULTRA-LOW NOISE MULTI-GIGAHERTZ FREQUENCY COMBS AND APPLICATIONS IN MULTI-HETERODYNE DETECTION OF ARBITRARY OPTICAL WAVEFORMS

by

JOSUE DAVILA-RODRIGUEZ
B.S. Tecnologico de Monterrey, 2006

A dissertation submitted in partial fulfillment of the requirements
for the degree of Doctor of Optics
in the College of Optics & Photonics
at the University of Central Florida
Orlando, Florida

Spring Term
2013

Major Professor: Peter J. Delfyett Jr.

ABSTRACT

The construction and characterization of ultra-low noise semiconductor-based mode-locked lasers as frequency comb sources with multi-gigahertz combline-to-combline spacing is studied in this dissertation. Several different systems were built and characterized. The first of these systems includes a novel mode-locking mechanism based on phase modulation and periodic spectral filtering. This mode-locked laser design uses the same intra-cavity elements for both mode-locking and frequency stabilization to an intra-cavity, 1,000 Finesse, Fabry-Pérot Etalon (FPE). On a separate effort, a mode-locked laser based on a Slab-Coupled Optical Waveguide Amplifier (SCOWA) was built. This system generates a pulse-train with residual timing jitter of <2 fs and pulses compressible to <1 ps. Amplification of these pulse-trains with an external SCOWA lead to 390 mW of average optical power without evident degradation in phase noise and pulses that are compressible to the sub-picosecond regime. Finally, a new laser is built using a 10,000 Finesse Fabry-Pérot Etalon held in a vacuum chamber. The fluctuations in the optical frequency of the individual comb-lines over time periods longer than 12 minutes are shown to be significantly reduced to <100 kHz in a measurement that is limited by the linewidth of the reference source.

The use of these comb sources as local oscillators in multi-heterodyne detection of arbitrary optical waveforms is explored in three different cases. 1) Sampling of mode-locked pulses, 2) sampling of phase modulated continuous wave light and 3) periodically filtered white light. The last experiment achieves spectral interferometry with unprecedented resolution.

"The ancient teachers of this science," said he, "promised impossibilities and performed nothing. The modern masters promise very little; they know that metals cannot be transmuted and that the elixir of life is a chimera but these philosophers, whose hands seem only made to dabble in dirt, and their eyes to pore over the microscope or crucible, have indeed performed miracles. They penetrate into the recesses of nature and show how she works in her hiding-places. They ascend into the heavens; they have discovered how the blood circulates, and the nature of the air we breathe. They have acquired new and almost unlimited powers; they can command the thunders of heaven, mimic the earthquake, and even mock the invisible world with its own shadows."

- M. Waldman (*Frankenstein*)

A mis padres

A Gabo, Becky y Toño

A la flaquita

ACKNOWLEDGMENTS

I owe many thanks to Professor Peter Delfyett for the opportunity to play a small part in his group. Without his seemingly infinite energy and his truly endless thirst for the next best system none of what follows would have been possible. Working in the Ultrafast Photonics group has been a true delight and the experience I've gained has shaped the way I approach problems, reflect upon them and focus on a possible solution. I can only hope that the next hundred or so pages are a faithful image of the group's philosophy and work ethic. The members of the group that I had the privilege to overlap with are: Dr. Frank Quinlan, Dr. Sarper Ozharar, Dr. Ji-Myoung Kim, Dr. Sangyoun Gee, Dr. Ibrahim Ozdur, Dr. Dimitrios Mandridis, Dr. M.U. Piracha, Dr. Nazanin Hoghooghi, Chuck Williams-Butt, Sharad Bhooplapur, Abhijeet Ardey, Dat Nguyen, Marcus Bagnell, Edris Sarailou, Anthony Klee and Kristina Bagnell. Other colleagues at CREOL that deserve a special mention: Andrew Sims, Andi Eisele, Alessandro Salandrino, Kyle Douglass, Armando Pérez, Enrique Antonio.

I thank Frank for walking me through the first few experiments and for sharing insights and ideas even today, many years after he left the group. Ibrahim was always up for hearing my dispersed and wavy arguments and carefully shooting them down. Dr. Dimitrios Mandridis was the best person to test argumentative endurance with. Chuck was a great lab partner and the greatest pun-master. Nazanin was a wonderful colleague and a better friend. She was always willing to listen and the best at pushing me to do more when I was discouraged.

Finally, I would like to credit the prompt availability of caffeine in CREOL with keeping me awake through the whole experience.

TABLE OF CONTENTS

LIST OF FIGURES IX

CHAPTER 1 : INTRODUCTION 1

1. Applications of frequency combs 1

Frequency domain applications *2*

Time domain applications *5*

2. Harmonically mode-locked lasers 6

3. Semiconductor-based mode-locked lasers as frequency comb sources 11

CHAPTER 2 : PHASE NOISE MEASUREMENT TECHNIQUES 12

1. Signal representation 12

2. Absolute, relative and residual phase noise 13

CHAPTER 3 : A MODE-LOCKED LASER STABILIZED TO AN INTRACAVTITY ETALON USING PHASE MODULATION AND PERIODIC OPTICAL FILTERING 19

1. Experimental setup and operation principle 20

2. Experimental results 25

3. Conclusions 29

CHAPTER 4 : A MODE-LOCKED LASER USING A SLAB COUPLED OPTICAL WAVEGUIDE AMPLIFIER (SCOWA) AS A GAIN MEDIUM 30

1. Experimental setup 31

2. Laser characterization 33

All SMF Cavity *33*

Dispersion compensated cavity *37*

3. Conclusions 39

CHAPTER 5 : ALL-DIODE AMPLIFICATION OF 10 GHZ PULSE-TRAINS 41
1. Overall MOPA system 42
2. Experimental results 43
3. Conclusions 47
CHAPTER 6 : FREQUENCY STABILITY OF A MODE-LOCKED LASER WITH A 10,000 FINESSE FABRY-PEROT ETALON 49
1. Experimental setup 49
2. Experimental results 51
3. Amplified spontaneous emission suppression as a function of filter Finesse 56
4. Conclusions 57
CHAPTER 7 : APPLICATION OF FREQUENCY COMBS IN MULTI-HETERODYNE MEASUREMENTS. PART I: THEORY 58
1. Conceptual description 60
2. Heterodyne detection of bandlimited white light and periodically filtered white light 64
CHAPTER 8 : APPLICATION OF FREQUENCY COMBS IN MULTI-HETERODYNE MEASUREMENTS. PART II: EXPERIMENTAL RESULTS 69
1. Mode-locked pulses 69
2. Phase modulated light 73
3. White light and periodically filtered white light 78
REFERENCES 82

LIST OF FIGURES

Figure 1.1: Frequency domain applications of frequency combs. (a) Calibration of stellar spectrograms and (b) Direct frequency comb spectroscopy using a second frequency comb as a local oscillator. 4

Figure 1.2: Optical arbitrary waveform generation using frequency comb from a mode-locked laser. 5

Figure 1.3: Photonically-sampled analog-to-digital converter. The mode-locked pulse-train acts as the sampling gate in the ADC setup. 6

Figure 1.4: Mode-locking through loss modulation. (a) Fundamentally and (b) harmonically mode-locked lasers..... 7

Figure 1.5: Mode-locked pulse-train and the corresponding spectrum. Notice that the f_{ceo} has been chosen to be ¼f_{rep}, which can also be seen in the pulses where the peak of the carrier coincides with the peak of the envelope after four pulses. 8

Figure 1.6. Harmonic mode-locking picture from the perspective of interleaved pulse-trains. In the top two panels a set of identical pulses are interleaved and perfect coherence makes 3 out of every 4 comb-lines destructively interfere. In the bottom panels small static phase shifts are introduced in each pulse-train, generating a periodic pattern in the frequency domain but without the destructive interference. 10

Figure 2.1: Noise measurement schemes. (a) Relative noise measurement by comparing two independent oscillators and (b) residual noise measurement. 14

Figure 2.2: Frequency discriminator technique for absolute noise measurements 16

Figure 2.3: Frequency discriminator transfer function for two different delays..... 18

Figure 3.1: Experimental setup. CIR: Circulator, DBM: Double Balanced Mixer, FPE: Fabry-Pérot Etalon, ISO: Isolator, LPF: Low-Pass Filter, OC: Output Coupler, PC: Polarization Controller, PD: Photodetector, PID: Proportional-Integral-Diferential Controller, PM: Phase Modulator, PS: Phase Shifter, PZT: Piezoelectric Transducer (Fiber Stretcher), SOA: Semiconductor Optical Amplifier 21

Figure 3.2: Phase modulation sidebands (black) and FPE transmission peaks (red). The mode-locking occurs due to the combination of phase modulation and periodic spectral filtering. The Finesse of the cavity for this plot is F = 100 and the depth of modulation β = 1.84 rad, for illustration purposes. 22
Figure 3.3: Measurement of the depth of modulation in the mode-locked laser. The black (red) dots show the expected amplitudes for depth of modulation β = 1.85 rad (2.02 rad). 23
Figure 3.4: Pound-Drever-Hall error signals for several depths of modulation and driving frequencies. These calculations include the effects of the interaction of higher-order sidebands with the Fabry-Pérot cavity. 24
Figure 3.5: Measurement of the dynamic PDH slope. (a) Real-time spectrogram and, (b) recovered peak frequency. The laser remains locked throughout the measurement. An error signal slope can be calculated from the size of each step, and has been calculated to be ~67 mV/MHz. 25
Figure 3.6 – Laser characteristics. (a) Optical spectrum, (b) High-resolution optical spectrum, (c) Photodetected pulse-train and, (d) Photodetected RF tone. 26
Figure 3.7 – (a) Spectrogram and, (b) a single RF trace of the heterodyne beat between a continuous-wave laser and one combline of the mode-locked laser. An upper bound to the frequency stability and the linewidth of the laser comblines can be set from these measurements. 27
Figure 3.8 – Phase noise measurement setup using a regenerative frequency divider. 28
Figure 3.9 – Phase noise power spectral density of the frequency divided radio-frequency tone and integrated timing jitter. The integrated timing jitter is the same as in the 10.285 GHz signal. 28
Figure 4.1. Mode-locked laser using a SCOWA and an intra-cavity Fabry-Pérot Etalon. CIR: Circulator, DBM: Double Balanced Mixer, FPE: Fabry-Perot Etalon, ISO: Isolator, LPF: Low-Pass Filter, OC: Output Coupler (Variable), PC: Polarization controller, PD: Photodetector, PID: Proportional-Integral-Differential Controller, PM: Phase Modulator, PS: Phase Shifter, PZT: Piezoelectric Transducer (Fiber Stretcher), SOA: Semiconductor Optical Amplifier (SCOWA), VOD: Variable Optical Delay 32

Figure 4.2 – (a) Optical spectrum and (b) High-resolution optical spectrum of a single combline. 34
Figure 4.3 – Optical frequency stability measurement via multi-heterodyne detection with a similarly built laser. (a) Schematic of the experimental setup, (b) Conceptual description of the multi-heterodyne process and, (c) recorded real-time spectrogram..... 35
Figure 4.4 – Photodetected pulse-trains (a) directly out of the laser and (b) after external compression. (c) and (d) show the autocorrelation traces from the pulse-trains in (a) and (b) respectively. 35
Figure 4.5 – RF tones of the photodetected pulse-trains. 36
Figure 4.6 – (a) Amplitude and (b) phase noise of the 10.287 GHz pulse-train..... 37
Figure 4.7. (a) Optical spectrum of a dispersion compensated laser cavity. (b) Heterodyne beat-note between a cw laser and a single comb-line. Also shown in (b) are Lorentzian lineshapes with 1 kHz and 2 kHz FWHM linewidth. 38
Figure 4.8. Autocorrelation traces. (a) A comparison of all the compressed autocorrelation traces in black, from all-SMF cavity, in blue from dispersion compensated cavity and in red, the calculated transform-limited pulse autocorrelation. (b) A 10 ps span plot showing only the red and blue traces..... 38
Figure 4.9. Residual phase noise measurements. The left axis shows the residual phase noise for (i) this chapter with the all-anomalous dispersion cavity and (ii) the dispersion compensated cavity; (iii) a similar laser with a commercially available gain medium [50] and (iv) absolute noise of the mode-locking source for all cases. The noise floor shown corresponds to measurement (i), but it is comparable in the other cases. The right axis in shows the integrated timing jitter for curves (i) and (ii) 39
Figure 5.1. Overal MOPA system built in the laboratory. The diagnostics box shown in the dashed box contains standard diagnostics equipment and it is kept as a unit during the experiments. Phase noise measurements are performed using an attenuated beam both to protect the photodetector and to match the amount of power used from the original pulse-train. The dashed box before the amplifier is an optional dispersion stage used to compress the pulses before amplification. 43

Figure 5.2. Gain measurements with pulses directly from the cavity and after compression. On the left side, autocorrelation traces of the pulses input to the amplification stage. On the right side a plot of Gain vs. Output power for the long (short) pulses in black (red). 44
Figure 5.3. Optical spectra of the amplified pulse-trains, measured at different output powers. Amplification of (a) long and (b) short pulses. 45
Figure 5.4. Pulse autocorrelation traces before and after amplification. (a) Amplifying pulses directly from the oscillator and subsequently compressing and (b) amplifying compressed pulses. 46
Figure 5.5. Comparison of compressed pulse autocorrelations before (red) and after (blue) amplification. 46
Figure 5.6 (a) Phase and (b) amplitude noise measurements for the pulse-trains before (black) and after (red) amplification 47
Figure 6.1. Schematic of the mode-locked laser utilized in this experiment. CIR: Circulator, DBM: Double Balanced Mixer, DCF: Dispersion Compensating Fiber, FPE: Fabry-Pérot Etalon, IM: Intensity Modulator, ISO: isolator, OC: output coupler, PC: Polarization controller, PD: Photodetector, PBS: Polarizing Beam Splitter, PM: Electro-optic Phase Modulator, PZT: Piezoelectric Fiber Stretcher, SOA: Semiconductor Optical Amplifier, VOD: Variable Optical Delay. The PBS used to multiplex the error signal is a bulk component. The FPE is kept in a vacuum and temperature stabilized enclosure. 51
Figure 6.2. Characterization of the laser output. (a) Optical Spectrum measured at port B (black) and port C (red). (b) Autocorrelation traces with the pulses passing through ~20 m of SMF and ~90 m of SMF. In blue, the calculated transform-limited autocorrelation. 52
Figure 6.3. Multi-heterodyne experimental setup. RT-RFSA: real time Spectrum Analyzer. 53
Figure 6.4. Single trace of the multi-heterodyne spectrum. Each comb-line is clearly resolved. The following measurements are the result of tracking the 14 comb-lines in the blue box. 54
Figure 6.5. Long term tracking of the comb-line frequency. The data on the left side was taken on Dec-13-2012 and on the right on Dec-14-2012. The laser operated continuously but it had to be relocked several times in between. The plotted data shows the beat-note centroid and the error

bars correspond to ±1σ. Notice that the centroid always remains within a 100 kHz window and the average value of σ is ~80 kHz..... 55
Figure 6.6. Statistics of the beat-note centroid positions. 2xσ is plotted in black squares and the maximum observed deviation over 12 minutes in red circles. Notice that even the maximum observed deviations are within one beat-note line-width. 56
Figure 6.7. Broadband ASE suppression for a mode-locked laser using (a) 1,000 Finesse and (b) 10,000 Finesse etalons. 57
Figure 7.1 – Conceptual picture of the multiheterodyne detection with a large repetition rate detuning. (a) Time domain depiction of the process. Notice the pulse walk-off between the LO and the signal under test. (b) Frequency domain picture in the optical domain and (c) the photodetected spectrum of the superposition of the two optical combs. The highest frequency combline pair (green) illustrates the aliasing effect. This is illustrated by the shaded areas underneath the frequency axis as well, with an overlapping region. Also note the difference in scales between the optical and RF frequency axes. 61
Figure 7.2 – Conceptual experimental setup for white light photocurrent interferometry. 67
Figure 7.3 – Simulation results. (a) Optical spectra. (b) Photocurrent interference for a fixed 20 ns delay 68
Figure 8.1 – (a) Optical spectra of the mode-locked comb sources. (b) Photodetected RF spectrum. (c) Smaller span of the RF spectrum. 71
Figure 8.2 – Time domain RF waveforms after downconversion as the 10.24 GHz mode-locked comb experiences different amounts of dispersion. 72
Figure 8.3 – Experimental setup. Amp: amplifier, BPF: bandpass filter, FC: frequency comb, CW: CW laser, LPF: low-pass filter, OC: optical coupler, PC: polarization controller, PD: photodetector, PM: phase modulator, PS: phase shifter, RFC: RF coupler, RFS: RF synthesizer, VA: variable attenuator. 74
Figure 8.4 – (a) Optical spectra of the phase-modulated CW light and the reference comb. (b) Photodetected RF spectrum. 74
Figure 8.5 – (a) Time domain waveforms, the red trace is displaced ~1/2 a period with respect to the black trace. (b) FFT of the fullwaveform. (c) FFT and spectral phase of a 1.6 μs segment of

the waveform. A constant offset and a linear trend have been removed from the phase plot. Only the phase values where the FFT has significant power are shown. The inset plot shows the errors of the phase compared to the theoretically expected values. 75
Figure 8.6 – Instantaneous frequency of the photodetected waveform. RF on the left y axis and optical in the right axis. Notice the compression between the two scales. The rms and mean absolute error are indicated in the figure. The fit errors are ~5% of the full range. 76
Figure 8.7 – Fitted time domain waveform. Notice that after a carrier frequency shift and bandwidth decompression, this corresponds exactly to the phase-modulated optical waveform. 77
Figure 8.8 – Multiheterodyne white light interferometry. (a) Optical spectra of the periodically filtered white light (blue) and the mode-locked laser (red). (b) RF spectra of the interfering photocurrents of the downconverted white light. 79
Figure 8.9 – Spectral interference of downconverted incoherent light. (a) Experimental setup. (b) Sampled RF waveforms. (c) Power spectra of the sampled waveforms. (d) Spectral interference with superposed transfer function of a spectral interferometer (red). 80
Figure 8.10 – Heterodyne photocurrent interferometry. (a) Experimental setup. (b) Calculated interferometry spectrogram. (c) Measured interferogram. 81

CHAPTER 1 : INTRODUCTION

Frequency combs have revolutionized a number of fields in experimental physics, metrology and engineering that their importance can hardly be overstated. A frequency comb, as produced by a femtosecond mode-locked laser, consists of a large (10^3 - 10^5) array of equally spaced, phase-locked narrow frequency components [1,2]. By controlling only two parameters, namely, the frequency spacing and the carrier-envelope offset frequency, every combline frequency can be known with sub-Hz accuracy [2,3]. It is this capability makes comb sources invaluable for a number of applications. This introduction is organized in three sections: the first enumerates and briefly describes some of the applications of frequency combs, making an attempt at pointing out which applications benefit from high repetition rate pulse-trains or widely spaced frequency combs, the second one presents a more detailed description of the frequency comb itself, as produced by a mode-locked laser, with emphasis on harmonically mode-locked lasers, and the last section contains a short review of recent advances in semiconductor-based lasers and frequency comb sources.

1.Applications of frequency combs

The range of applications of optical frequency combs is extremely broad and only a short review is presented here. Depending on whether the periodicity of the electric field or the spectral purity and precise equidistancy of the spectral lines is of use to the application at hand one can very

broadly (and somewhat artificially, since both characteristics are intimately connected) categorize the applications of frequency combs into frequency-domain applications and time-domain applications.

Frequency domain applications

In high precision spectroscopy, an optical frequency comb is used to accurately determine the optical frequency of the atomic or molecular transition by acting as a link between a microwave frequency standard and the narrow line-width laser that interrogates said transition [4]. This ability to essentially count the optical cycles permits extremely precise determinations of the transition frequencies in single ions [5] and cold atomic beams [6].

This process can be used in reverse using an atomic resonance with very narrow linewidth (known as a clock transition) as a primary frequency standard and a self-referenced frequency comb is used to count the optical cycles of the laser interrogating the resonance. The system is then essentially an optical clock. Optical clocks are expected to perform orders of magnitude better than the current fountain Cs clock [7,8].

The possibility of extending the spectral coverage of frequency combs via nonlinear processes also enables molecular spectroscopy in the mid-ir region where the rotational-vibrational molecular fingerprints lie [9–12]. Molecular fingerprinting with frequency combs could bring about simple and multiplexed stand-off detection as well as trace gas detection with unprecedented sensitivities. Nonlinear processes also allow generation of coherent light at the other end of the electromagnetic spectrum. This is done by generating extremely high peak electric fields via the control of the carrier-envelope phase slip, which enables coherent high-

harmonic generation and has resulted in the generation of extreme UV combs [13] which can potentially be used for spectroscopy on ionized Helium, extending the tests of Quantum Electrodynamics [14,15] to a new level of precision.

In the history of scientific progress, the advent of more accurate measurement tools (in this case, time-keeping and frequency metrology tools) has been accompanied by new scientific discoveries and technological developments. As an example in fundamental physics, the drift or fluctuation (or the lack thereof) of fundamental constants can be tested for [16] and more extreme tests of special and general relativity can be performed by following the changes in the speed of distant galaxies over time. One technique for detection of extrasolar planets requires the ability to measure changes in Doppler shifts as small as 1 cm/s/yr [17]. For the measurement of small Doppler shifts in the emission spectra from distant stars, frequency combs provide a stable and absolutely calibrated frequency grid that the stellar spectrographs can be compared to. The absolute calibration provided by the comb allows for comparisons of spectrographs recorded at distant locations and over very long periods of time without loss of calibration. In essence, this procedure measures the “wobble” of a star that has an earth-like companion and thus hunt for possible inhabited extra-solar planets [18,19].

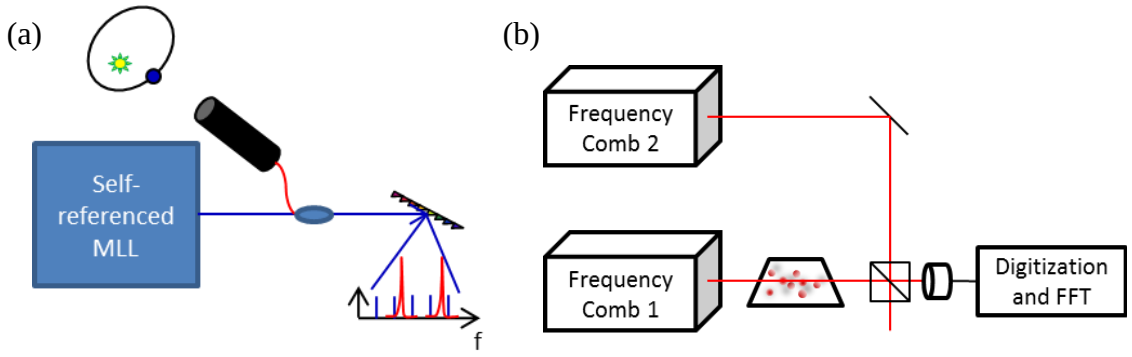

Figure 1.1: Frequency domain applications of frequency combs. (a) Calibration of stellar spectrograms and (b) Direct frequency comb spectroscopy using a second frequency comb as a local oscillator.

Precision length measurements can be significantly improved by the use of two frequency combs [20,21], where the coherence in both the RF and optical domains is used to implement a combined time-of-flight and interferometric measurement which increases the resolution without decreasing the ambiguity range at the same time. Multi-heterodyne techniques can be also applied to spectroscopy, using one of the combs as a probe while the second comb acts as a local oscillator to down-convert and sample the changes undergone by the probe beam. This powerful technique can simultaneously resolve the individual vibrational-rotational levels in gases and the signals can be coherently accumulated for very long times, significantly increasing the signal-to-noise ratio [22–26]. In this dissertation, the application of multi-heterodyne techniques will be extended to mutually incoherent sources with periodic spectral structures.

Optical communications also benefit from frequency combs by allowing the development of dense WDM modulation schemes where each combline is modulated individually, the comb recombined and transmitted through the network [27,28]. Individual lines of lasers with comb spacing in the order of 10 GHz can be spectrally separated and modulated with high-speed

modulators such that the full bandwidth between the comblines is filled. This same capability enables true arbitrary waveform generation [29], which can have an impact in LIDAR and RADAR technologies.

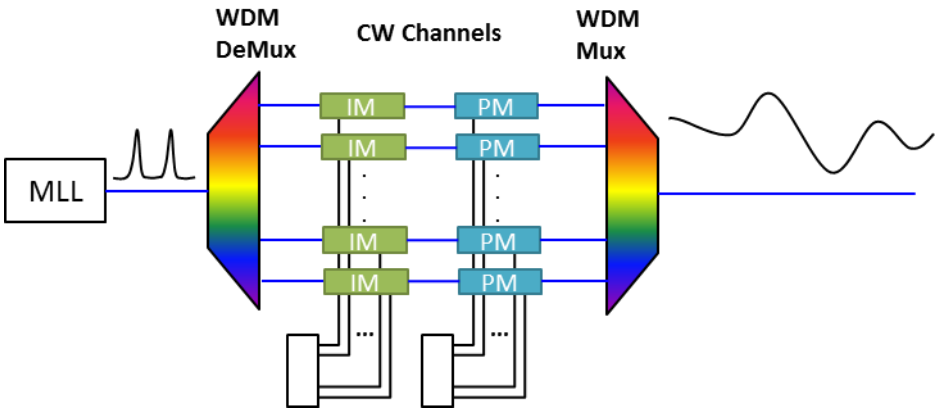

Figure 1.2: Optical arbitrary waveform generation using frequency comb from a mode-locked laser.

Time domain applications

The ultra-low timing and amplitude jitter of the pulse-trains produced from mode-locked lasers can have an impact on photonically-sampled analog-to-digital conversion [30,31], where the laser pulse acts as the sampling gate holding the value of the RF signal until it is converted into an electrical signal.

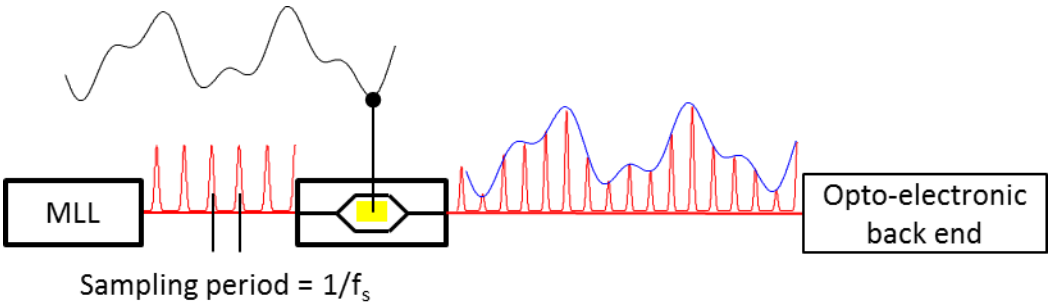

Figure 1.3: Photonically-sampled analog-to-digital converter. The mode-locked pulse-train acts as the sampling gate in the ADC setup.

More recently, frequency combs have been used in the generation of ultra-low noise microwave signals via optical frequency division [32–34]. This process requires a self-referenced mode-locked laser whose repetition rate is locked to an ultra-narrow linewidth continuous wave laser. The repetition rate of the mode-locked laser is then photodetected and band-pass filtered. The phase noise of these signals has been shown to be extremely low, since it divides the optical frequency by a number in the order of 10^4 to 10^6.

2. Harmonically mode-locked lasers

This section outlines some of the properties of the pulse-trains obtained from fundamentally and harmonically mode-locked lasers. This topic has been treated extensively in the literature [35–39] and only a brief summary is presented here. A picture of a typical loss-modulation setup for a mode-locked laser is shown in Figure 1.4, where the modulator in (a) is driven with a period equal to the round-trip time of the optical cavity or (b) at an integer submultiple of the round-trip time of the cavity. The pulses in case (b) have been color coded to show that they do not

originate from the regeneration of a single pulse, which gives rise to periodic noise patterns in the output pulse-train.

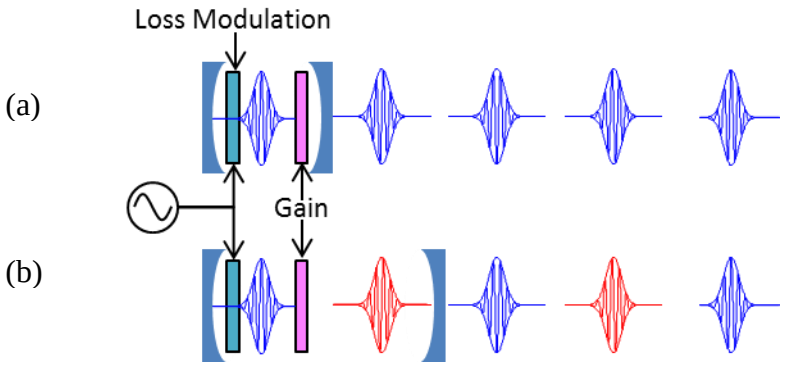

Figure 1.4: Mode-locking through loss modulation. (a) Fundamentally and (b) harmonically mode-locked lasers.

In a fundamentally modelocked laser, pulses are generated periodically and every pulse originates from the regeneration of a single pulse. Assuming a perfectly periodic pulse-train, its electric field can be written as:

$$E(t) = \sum_{n} \hat{E}\left(t - nT_{rep}\right) e^{-i\omega_c (t - nT_{rep})}\, e^{-in\phi_{ce}} \tag{1.1}$$

where $\hat{E}\left(t - nT_{rep}\right)$ is the envelope of a single pulse. ϕ_{ce} is the carrier-envelope phase-slip and it arises from the difference between the phase and group velocities of the pulse. Fourier transformation gives a perfect frequency comb (comprised of delta functions) in the limit of an infinitely long pulse-train, as follows:

$$E(\omega) = \tilde{E}(\omega - \omega_c) \sum_k \delta(\omega - 2\pi k f_{rep} - f_{ceo}) \quad (1.2)$$

where $f_{rep} = \frac{1}{T_{rep}}$, and $f_{ceo} = \frac{\phi_{ce}}{2\pi} f_{rep}$, and $\tilde{E}(\omega)$ is the Fourier transform of the envelope of a single pulse. Therefore, the spectrum is an array of spectral lines located at frequencies equal to:

$$f_n = k \times f_{rep} + f_{ceo} \quad (1.3)$$

The ratio between f_{ceo}/f_{rep} essentially determines the number of periods ($1/f_{rep}$) that it takes for the waveform to be exactly identical, considering the optical carrier under the envelope.

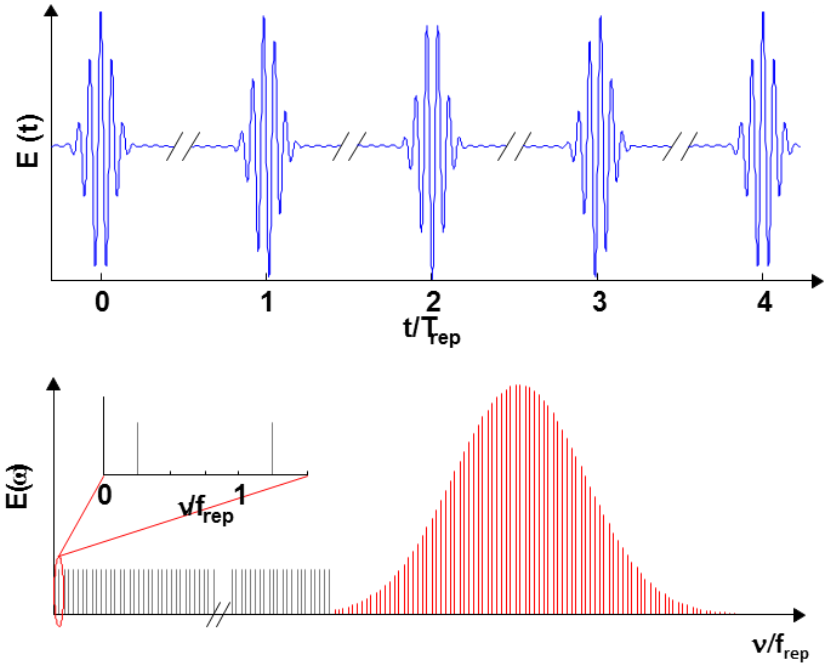

Figure 1.5: Mode-locked pulse-train and the corresponding spectrum. Notice that the f_{ceo} has been chosen to be ¼f_{rep}, which can also be seen in the pulses where the peak of the carrier coincides with the peak of the envelope after four pulses.

In a harmonically mode-locked laser, however, there is more than one pulse in the cavity at the same time (in the case of some of the lasers presented in future chapters, there are 1000's of pulses in the cavity). These pulse-trains originate from independent portions of spontaneous emission and are, in general, not correlated with each other. This property imposes a periodic noise pattern in the pulse-train with a periodicity equal to the cavity round-trip time. In this interpretation, the output pulse-train can be considered as the interleaving of multiple independent pulse-trains, each of which has the period of the cavity round-trip time. This in turn leads to a spectrum that consists of the summation of independent spectra with comblines spaced by the cavity fundamental frequency. This picture is shown in Figure 1.6. On the top left side a high repetition rate pulse-train is represented as the sum of multiple lower repetition rate pulse-trains. The pulse-trains are assumed to be identical with the exception of a time delay equal to $1/f_{rep}$ between them. This leads to a Fourier transform (top right) where each comb has a different linear phase slope (everything else is equal). Adding these spectra causes perfect destructive interference on 3 out of every 4 comb-lines, generating a comb spectrum at the repetition rate of the pulse-train. This ideal situation is not met in harmonically mode-locked lasers both because of the presence of dispersion and, more evidently, because each pulse-train is generated from an 'initial' burst of amplified spontaneous emission appearing in its time-slot and without correlation to the other pulse-trains. By assuming that each pulse-train has a random overall phase shift with respect to the other pulse-trains and adding the obtained spectra (Figure 1.6) the obtained spectrum has comb-line to comb-line spacing of f_{cav}. Evidently, there is an overall f_{rep} periodicity (both in amplitude and phase) on this comb. This accounts for the high-repetition rate intensity pattern while the electric field is periodic only with f_{cav}.

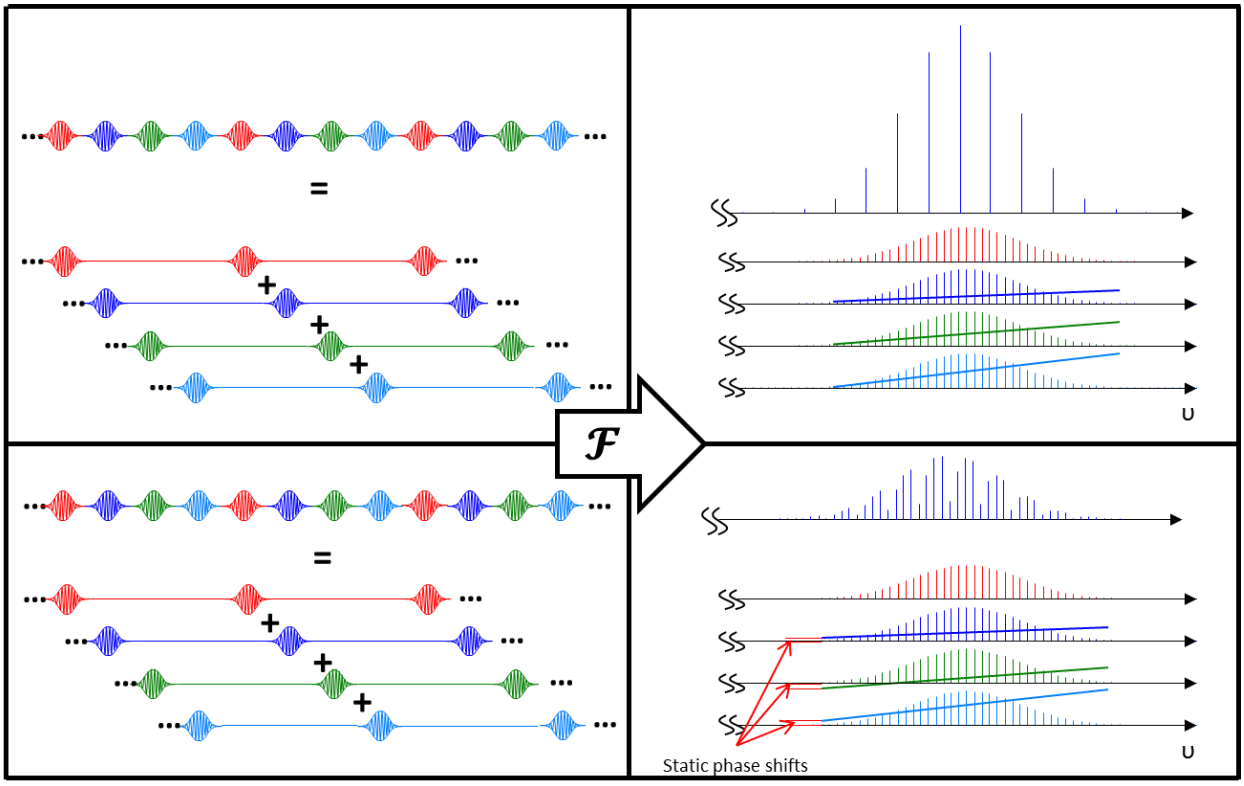

Figure 1.6. Harmonic mode-locking picture from the perspective of interleaved pulse-trains. In the top two panels a set of identical pulses are interleaved and perfect coherence makes 3 out of every 4 comb-lines destructively interfere. In the bottom panels small static phase shifts are introduced in each pulse-train, generating a periodic pattern in the frequency domain but without the destructive interference.

In the case of an actively mode-locked laser, one can draw a similar picture starting from the frequency domain due to the fact that the loss modulation imposes a condition which couples comb-lines that are f_{rep} away from each other. Ultimately, this picture leads to a set of pulse-trains whose repetition rate is equal to f_{rep} and which add to generate a pulse-train at the same repetition rate but whose electric-field phase is periodic with f_{cav}.

3.Semiconductor-based mode-locked lasers as frequency comb sources

Semiconductor-based mode-locked lasers can be very attractive as compact sources of picosecond pulses with high repetition rates in the fiber optic communication band of 1.5 μm [40]. Semiconductor laser media are also attractive because they are electrically pumped, which contributes to the compactness of the system, as well as to its wall-plug efficiency. Although the integration of light emitting semiconductor chips with CMOS compatible technologies (to achieve full optical-electronic integration) remains a field that faces many challenges, significant improvements have been made over the past few years [41,42] and it can certainly be expected that more integrated devices will be developed in the near future.

Ultra-stable and ultra-low noise performance of semiconductor lasers can be achieved with external cavities, through careful cavity engineering and design. Long term stabilization of pulse repetition rate and optical frequency has been demonstrated through the use of intra-cavity etalons and Pound-Drever-Hall control loops [35,43].

Finally, another advantage of semiconductors-based lasers is that their operation can be extended to other wavelength regimes via bandgap engineering.

CHAPTER 2 : PHASE NOISE MEASUREMENT TECHNIQUES

This chapter will introduce some of the techniques used in the measurement of fluctuations in periodic signals. Several techniques previously developed in the domain of microwaves [44–46] can be imported and adapted to the field of optics since the photodetected current corresponds to a microwave electrical signal that carries the timing and amplitude jitter of the envelope of the original pulse-train. Other methods, such as frequency discriminators, benefit from optics and can be improved and used in a much broader spectral region using optical fibers and interferometric techniques [47,48], as will be discussed below. In general, it is relevant to understand the significance of noise, its fundamental limits and the techniques to measure and characterize it.

1.Signal representation

A narrow-band signal can be represented as a sinusoid whose amplitude and phase are allowed to present small deviations from the ideal case. This representation can be done in a Cartesian manner using in-phase and quadrature components or, in a phasor fashion, using amplitude and phase. The latter is convenient since the fluctuations in these quantities represent the amplitude and timing jitter of the signal. Thus, an almost perfect sinusoid can be represented as:

$$v(t) = \Re\left\{[1+\alpha(t)]e^{j\left(\omega_0 t+\varphi(t)\right)}\right\} = [1+\alpha(t)]\cos\left(\omega_0 t+\varphi(t)\right) \quad (2.1)$$

where α(t) represents the fractional amplitude fluctuations and φ(t) the phase fluctuations. The signal is written normalized to unitary amplitude and an overall constant phase has been omitted

by setting the time origin at one of the maxima of the signal. Although both amplitude and phase noise are assumed to be small, phase noise and amplitude noise are fundamentally different in that, for long observation times, phase noise diverges, whereas amplitude noise is bound in every oscillator by some limiting mechanism.

The spectral content of such a signal can be obtained through its Fourier transform as follows:

$$\tilde{v}(\omega) = \frac{1}{\sqrt{2\pi}} \int_{-\infty}^{\infty} [1 + \alpha(t)] e^{j\varphi(t)} e^{-j(\omega-\omega_0)t} dt \qquad (2.2)$$

Assuming $\varphi(t) << 1$ radian and $\alpha(t) << 1$, expanding the phase noise from the exponential and ignoring all higher-order noise terms, we can rewrite this integral as

$$\tilde{v}(\omega) = \frac{1}{\sqrt{2\pi}} \int_{-\infty}^{\infty} [\alpha(t) + j\varphi(t)] e^{-j(\omega-\omega_0)t} dt \qquad (2.3)$$

where it is evident that the first-order noise terms appear as sidebands on a delta function centered at ω_0. Amplitude noise and phase noise appear as an in-phase and in-quadrature addition, respectively. Higher order phase noise terms as well as mixing products do appear in the expansion, but can usually be ignored provided that the noise is small, which is always the case for a high-quality oscillator.

2.Absolute, relative and residual phase noise

Amplitude and phase fluctuations can be measured in several ways that are relevant depending on the particular application. Power spectral densities of either $\alpha(t)$ or $\varphi(t)$ are usually measured

using a radio-frequency spectrum analyzer (RFSA) or a similar device. Measuring directly at the carrier frequency has some drawbacks: (1) an RFSA measures power spectral densities, combining phase and amplitude fluctuations, (2) the noise sidebands are usually extremely small compared to the carrier such that the dynamic range of the RFSA is not enough, (3) the IF filter bandwidth is usually much larger than would be desired and (4) the swept voltage controlled oscillator inside the RFSA can be too unstable for the task. Down-conversion with a mixer solves most of these problems by allowing the mixing to be done with an arbitrary phase angle (separating AM and PM noise) and producing the noise sidebands at close-to-zero frequencies, which makes it easy to accurately sample and analyze together with a second harmonic term which can be easily filtered out. Since timing jitter is probably the most important parameter in the stability of an oscillator, the descriptions given here will be centered on phase noise. Also, the experimental setups described are conceptual in nature and some practical issues will be discussed later.

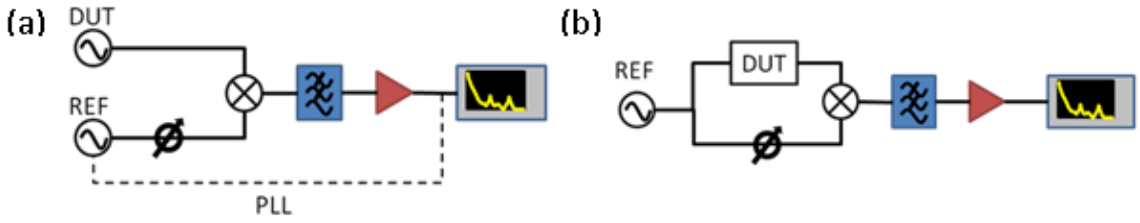

Figure 2.1: Noise measurement schemes. (a) Relative noise measurement by comparing two independent oscillators and (b) residual noise measurement.

For any two input signals with the same frequency and a constant phase of $\pi/2$, a mixer will give a voltage that is proportional to the difference in the phase fluctuations between the two arms (see Figure 2.1):

$$V(t) \propto \varphi_{\mathrm{DUT}}(t) - \varphi_{\mathrm{REF}}(t) \tag{2.4}$$

The power spectral density of this signal would then be:

$$S_V(\omega) = S_{\varphi_{\mathrm{DUT}}}(\omega) + S_{\varphi_{\mathrm{REF}}}(\omega) - 2\Re\{\mathcal{F}\{\varphi_{\mathrm{DUT}}(t) \star \varphi_{\mathrm{REF}}(t)\}\} \tag{2.5}$$

where the last term in the expression is the Fourier transform of the cross correlation of the phase fluctuations of both sources and for uncorrelated devices this term vanishes. Each of the first two terms represents the absolute noise of each signal and it measures the deviation of the phase of the signal from that of a perfect sinusoid, while the measured quantity, $S_v(\omega)$, is known as the relative noise between the sources. The ultimate performance of an oscillator is given by its absolute noise. Figure 2.1 (a) shows a conceptual measurement setup of this type. If the reference oscillator's phase noise is much lower than that of the device under test (DUT) then the output noise is approximately that of the DUT. If they are similar, then the noise is twice that of a single oscillator. It is evident from Eq. (2.4) that in a residual noise measurement the fluctuations that are common to both oscillators will interfere due to coherent addition of signals. For very short path differences or low Fourier frequencies, these quantities destructively interfere and vanish.

Residual noise is used to mean the uncorrelated noise added by the DUT. In the case of mode-locked lasers this includes spontaneous emission and the environmental noise that modifies the properties of the laser cavity. Figure 2.1 (b) shows a residual noise measurement, where it is evident that the fluctuations of the reference source will cancel out, as long as they are not filtered by the DUT. If the DUT includes a high-finesse filter, then the measurement will yield artificially high residual noise in the spectral regions where the phase noise in the DUT arm is

lower than the phase noise in the reference arm [49]. The total noise of a two-port device would be given by:

$$\varphi(t) = h(t) \otimes \varphi_{ref}(t) + \varphi_{res}(t) \quad (2.6)$$

where h(t) is the impulse response of the DUT and $\varphi_{res}(t)$ is the residual (uncorrelated) noise added by the device. The power spectral density of the output of the mixer would then be:

$$S_V(\omega) = [1 - H(\omega)] S_{\varphi_{ref}(\omega)} + S_{\varphi_{res}(\omega)} \quad (2.7)$$

The cross correlation term was omitted from Eq. (2.7) since the residual noise is by definition uncorrelated to the noise of the reference. From this equation it is also evident that in the spectral regions where H(ω) is flat, the output of the mixer is the residual noise of the device.

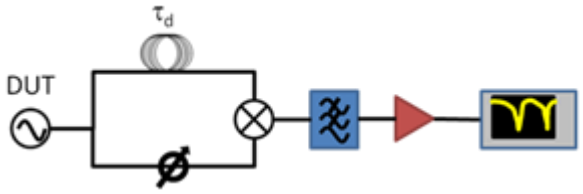

Figure 2.2: Frequency discriminator technique for absolute noise measurements

Measuring absolute noise can be challenging when there are no good frequency references on the frequency range of the oscillator under test. One technique mentioned above is using two similar oscillators under the assumption that each contributes half of the measured phase noise. Another possibility is using the three oscillator technique, where the measurement described by Eq. (2.5) is performed between the three possible combinations of three oscillators, and the phase noise of any one of them can be obtained from:

$$S_A(\omega) = \frac{1}{2}[S_{A,B}(\omega) + S_{A,C}(\omega) - S_{B,C}(\omega)] \quad (2.8)$$

The main disadvantage of the three oscillator method is that it requires the three oscillators of comparable quality. Another method for absolute noise measurements consists of the frequency discriminator or delay-line measurement, schematically shown in Figure 2.2. In this setup, the signal is mixed with a delayed version of itself, causing the noise at different frequency offsets to interfere in a periodic fashion [47,48]. It is easy to see that:

$$\mathcal{F}\{\varphi(t) - \varphi(t-\tau)\} = \frac{1}{2}[1 - e^{j\omega\tau}] \times \mathcal{F}\{\varphi(t)\} \quad (2.9)$$

From this equation, we can see that the phase noise of the oscillator and the power spectral density at the output of the mixer are related by:

$$S_V(\omega) = (1 - \cos\omega\tau) \times S_\varphi(\omega) \quad (2.10)$$

The frequency discriminator transfer function is shown in Figure 2.3. For this particular measurement system, it is advantageous to use a photonic (fiber) delay line because it minimizes the losses; it is practically immune to electromagnetic interference and can be very compact. It is important to note that the noise at low frequency offsets is severely attenuated due to the transfer function of the delay line. Thus, to measure long term stability of oscillator, long delay lines are required and high stability for these fiber coils must be ensured as well.

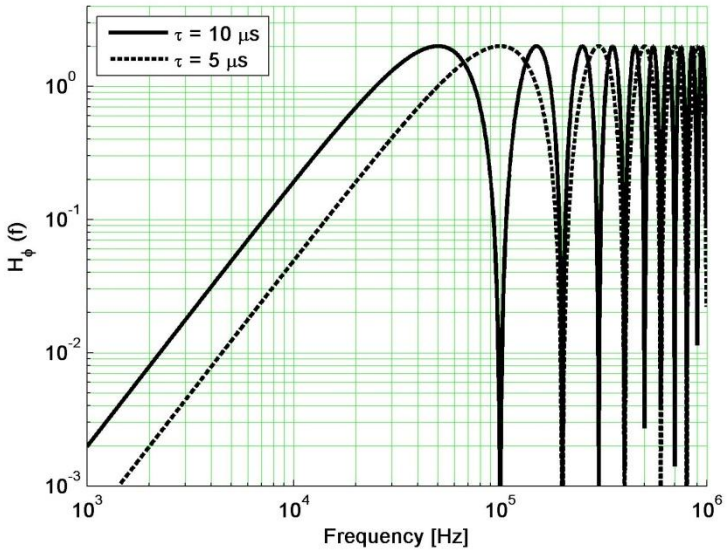

Figure 2.3: Frequency discriminator transfer function for two different delays.

A common figure of merit for the performance of oscillators is the integrated rms timing jitter, which can be calculated from the phase noise power spectral density through:

$$T_J = \frac{1}{2\pi f_{rep}} \sqrt{2 \int_{f_0}^{f_1} S_\phi(f) df} \qquad (2.11)$$

In the following chapters, the residual timing jitter of actively mode-locked lasers will be used as a figure of merit to assess the quality of the pulse-train as it compares to the mode-locked source.

CHAPTER 3 : A MODE-LOCKED LASER STABILIZED TO AN INTRACAVTITY ETALON USING PHASE MODULATION AND PERIODIC OPTICAL FILTERING

Both high repetition rate pulse-trains and frequency comb sources with multi-gigahertz combline-to-combline spacing are desirable for a multiplicity of applications [27,28]. Harmonically mode-locked lasers can directly provide high repetition rate pulse-train, but have the drawback that multiple cavity mode-sets may exist at the same time and this leads to periodic noise patterns in the output pulse-trains [35–37]. To overcome this issue, harmonically mode-locked lasers with an intra-cavity Fabry-Pérot etalon (FPE) as a high-finesse filter have been demonstrated and have shown good performance in regards to amplitude and phase noise of the output optical pulse-trains as well as the frequency stability of the individual comblines [50]. This architecture has the advantage that the long fiber cavity has a high quality factor, providing narrow longitudinal modes, while the FPE provides the wide mode-spacing. In these comb sources, the modes of the fiber cavity are stabilized to the intra-cavity FPE through a modified, multi-combline, Pound-Drever-Hall (PDH) scheme. The PDH stabilization loop typically requires an independent radio-frequency source in order to phase modulate a portion of the output optical comb and derive an error signal by probing the FPE resonance through a technique analogous to frequency modulation spectroscopy [51,52]. However, there is a trade-off between the optical power available as usable laser output and that used in the stabilization loop. Since the slope of the error signal increases with the optical power, using a larger fraction of the light in the stabilization loop results in a tighter lock, but this reduces the power available in the output

pulse-train. Increasing the output coupling makes more power available for the PDH loop at the expense of the laser's cavity quality factor.

Mode-locked lasers using phase modulation and an intra-cavity FPE have been demonstrated as a means for repetition rate multiplication [53,54]. These lasers operate by modulating at a sub-harmonic of the etalon's FSR. It is then the higher order side-bands that oscillate in the cavity, creating pulse-trains with a repetition rate that is a multiple of the driving frequency.

In this chapter, a mode-locked laser is presented in which both mode-locking and frequency stabilization are achieved using a single phase modulator and the intra-cavity etalon. Using the same intra-cavity elements for both purposes achieves a simplification of the feedback loop that is typically used, as compared to the one in reference [50]. It should be noted that in this setup (Figure 3.1), all of the intra-cavity power is used for the stabilization loop, which is roughly an order of magnitude larger than the output power, creating tighter lock while avoiding the trade-off with the available power at the output.

1.Experimental setup and operation principle

A commercially available semiconductor optical amplifier (SOA) is used as the gain medium and the phase modulator is driven at exactly one-half the free-spectral range (FSR) of the FPE. The etalon is built with an ultra-low expansion quartz spacer, is hermetically sealed to mitigate the effects of environmental fluctuations, and has FSR = 10.285 GHz and a Finesse of 1,000. The fiber cavity is 28 m long and is comprised entirely of standard single mode fiber. Mode-locking

is attained by the combination of high-depth phase modulation and the periodic spectral filtering provided by the etalon.

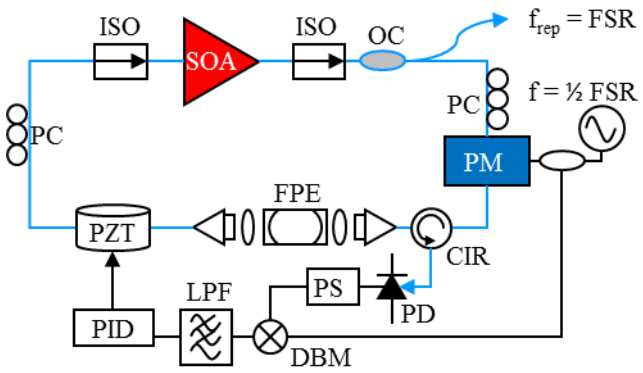

Figure 3.1: Experimental setup. CIR: Circulator, DBM: Double Balanced Mixer, FPE: Fabry-Pérot Etalon, ISO: Isolator, LPF: Low-Pass Filter, OC: Output Coupler, PC: Polarization Controller, PD: Photodetector, PID: Proportional-Integral-Diferential Controller, PM: Phase Modulator, PS: Phase Shifter, PZT: Piezoelectric Transducer (Fiber Stretcher), SOA: Semiconductor Optical Amplifier

The diagram in Figure 3.2 shows the phase modulation sidebands generated by the phase modulator and the transmission function of the FPE. Only the modes within the etalon transmission peaks are allowed to oscillate and become part of the mode-locked spectrum. Note that the transmitted modes are in phase with the main carrier and spaced by twice the modulation frequency, therefore the amplitude of the transmitted field is modulated at the FSR of the etalon. The reflected sidebands, (together with a portion of the carrier when it is off-resonance) are collected through a circulator and photodetected to generate a PDH error signal that is demodulated by mixing in quadrature with the driving signal. This signal is used to control the fiber cavity length via a piezoelectric fiber stretcher and keep the lasing frequency at the peak of the FPE transmission. The main advantages of the system simplification are: (1) the number of intra-cavity elements is reduced, reducing the footprint of the system and potentially leading to a

cavity design with lower loss, (2) an additional RF oscillator is not needed for the stabilization loop, and (3) the useful output power is increased since there is no need to use a portion of it in the stabilization loop.

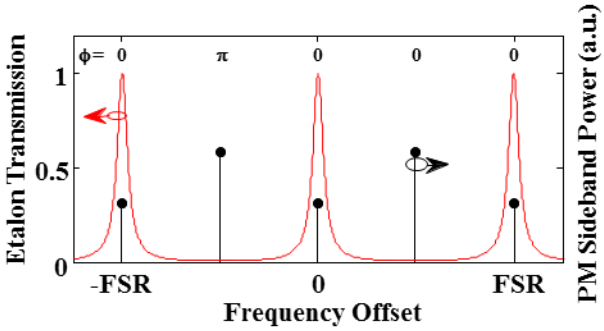

Figure 3.2: Phase modulation sidebands (black) and FPE transmission peaks (red). The mode-locking occurs due to the combination of phase modulation and periodic spectral filtering. The Finesse of the cavity for this plot is F = 100 and the depth of modulation β = 1.84 rad, for illustration purposes.

A few parameters must be optimized to obtain the desired laser performance. The depth of modulation was empirically optimized based on laser performance (optical bandwidth and pulse-train stability). Keeping the RF power to the phase modulator constant and using a CW laser, a measurement was performed to obtain the depth of modulation. The plot in Figure 3.3 shows the High Resolution optical spectrum of the output from the phase modulator. This measurement shows that the depth of modulation is between 1.85 and 2 rad. It is important to note that this range of depth of modulation is with certainty below the point (β = 2.405 rad) at which the carrier is suppressed and it is in fact close to the point where the first and second order sidebands have the same power. It was also found that the laser can mode-lock (and be PDH locked) at lower modulation indices, typically at the cost of narrower spectral bandwidth.

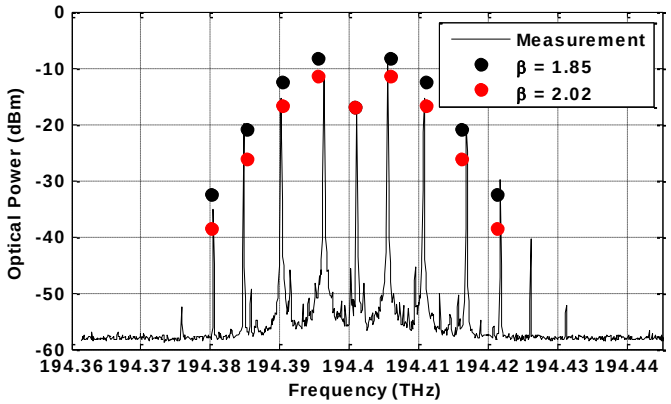

Figure 3.3: Measurement of the depth of modulation in the mode-locked laser. The black (red) dots show the expected amplitudes for depth of modulation β = 1.85 rad (2.02 rad).

The standard PDH stabilization scheme assumes a relatively low depth of modulation (to be able to consider only first order side-bands in the calculation) and that the generated side-bands are non-resonant. Neither condition is fulfilled in this setup because the depth of modulation is high, leading to considerable power in higher-order sidebands and, all the even order sidebands are resonant with the Fabry-Pérot cavity. For this reason, numerical calculations were performed to verify that an error signal could be obtained. Figure 3.4 shows the calculated error signals for several cases. To point out some of the interesting features of these calculations, notice that when the modulation index increases significantly (middle column) several structures appear from the interaction of the resonant even-order sidebands. Another interesting case is when the carrier is completely suppressed (β = 2.405), where no error signal is observed on resonance, signal that reappears as the modulation frequency reaches ½FSR, at which point the signal originates from the interaction of the ±2 sidebands.

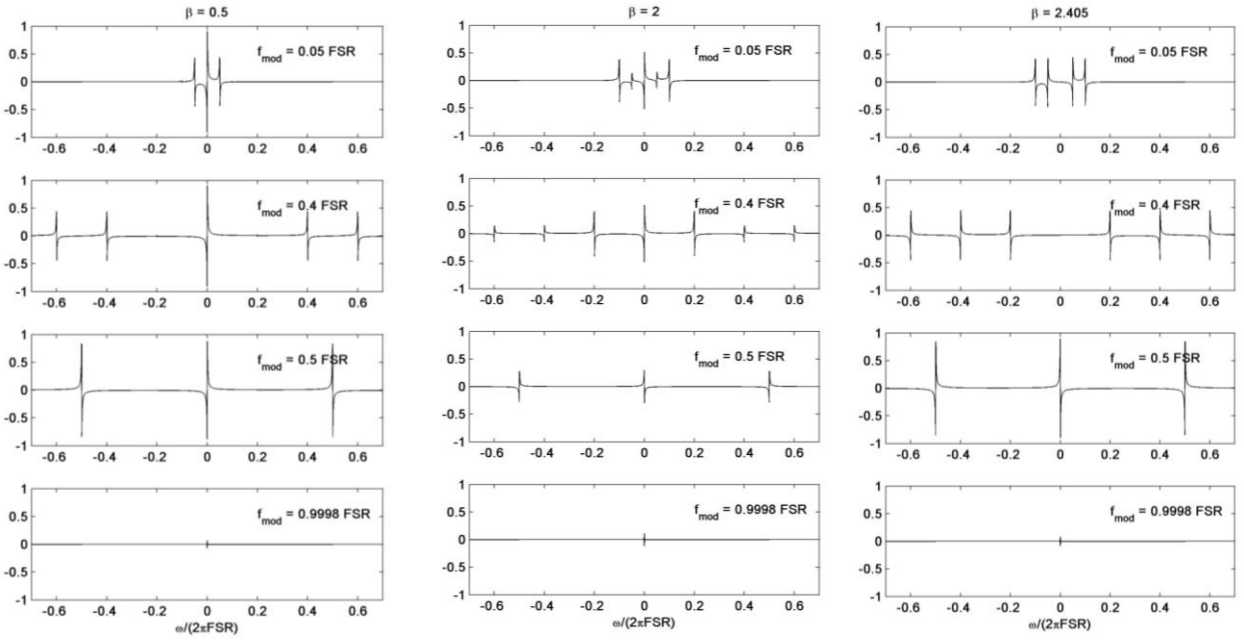

Figure 3.4: Pound-Drever-Hall error signals for several depths of modulation and driving frequencies. These calculations include the effects of the interaction of higher-order sidebands with the Fabry-Pérot cavity.

Another evident feature of the plots in Figure 3.4 is that the slope of the error signal is significantly reduced for the case that approximately matches the setup in the mode-locked laser under study ($\beta = 2$, $f_{MOD} = ½FSR$). Other dynamic effects that could come into play would be the interaction between multiple laser comblines. For this reason it was decided that an empirical study of the error signal had to be performed. Essentially, we measured the "dynamic slope" of the PDH error signal. To do this, a heterodyne beat between a mode-locked laser combline and a cw laser was observed while the locking point was manually changed in 10 mV steps (see spectrogram in Figure 3.5) and from this data, we calculated that the dynamic slope is ~67 mV/MHz. The total locking range is ~2MHz or ~20% of the FPE's -3dB linewidth.

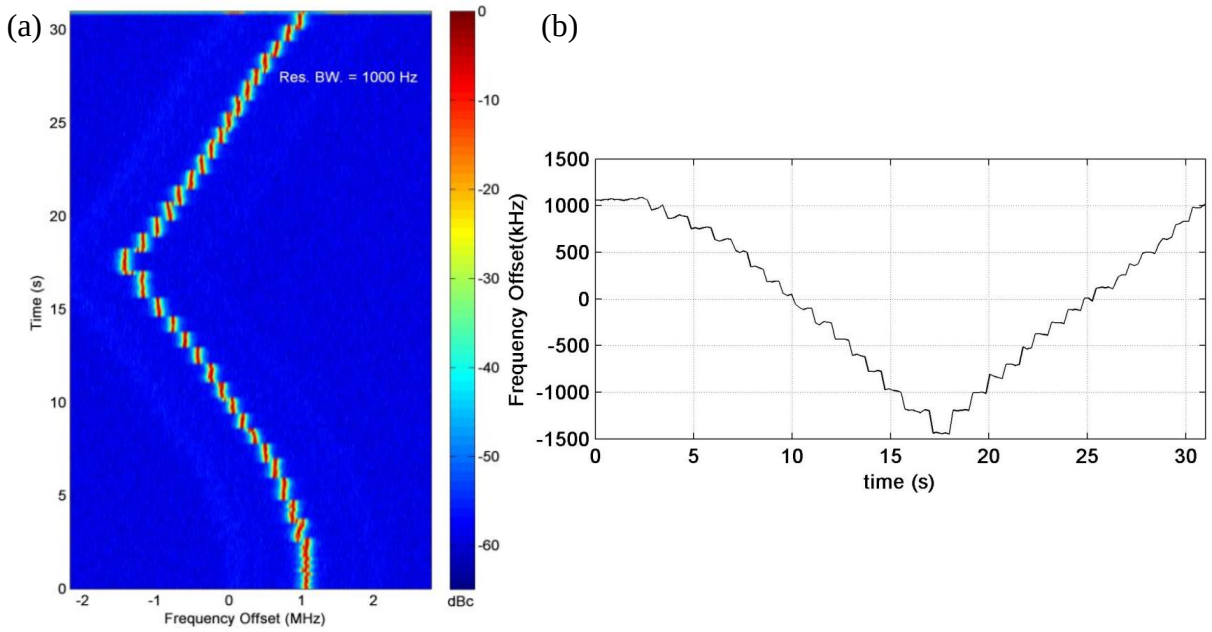

Figure 3.5: Measurement of the dynamic PDH slope. (a) Real-time spectrogram and, (b) recovered peak frequency. The laser remains locked throughout the measurement. An error signal slope can be calculated from the size of each step, and has been calculated to be ~67 mV/MHz.

2.Experimental results

The mode-locked laser output consists of a pulse-train with 10.285 GHz repetition rate and average power of ~5 mW. The optical spectrum is a comb of optical frequencies spaced by 10.285 GHz and has a 10 dB bandwidth of ~3 nm (Figure 3.6(a)). A high resolution trace of one combline is shown in Figure 3.6 (b). The modes spaced by the cavity fundamental (~7 MHz) are not visible in this measurement. The observed optical signal to noise ratio is 60 dB at a resolution bandwidth of 1 MHz. An average of 12 sampling oscilloscope traces of the corresponding pulse-train is shown in Figure 3.6 (c), using an oscilloscope with equivalent bandwidth of 30 GHz. The photodetected RF tone at 10.285 GHz in Figure 3.6 (d) has signal-to-noise ratio >115 dBc/Hz.

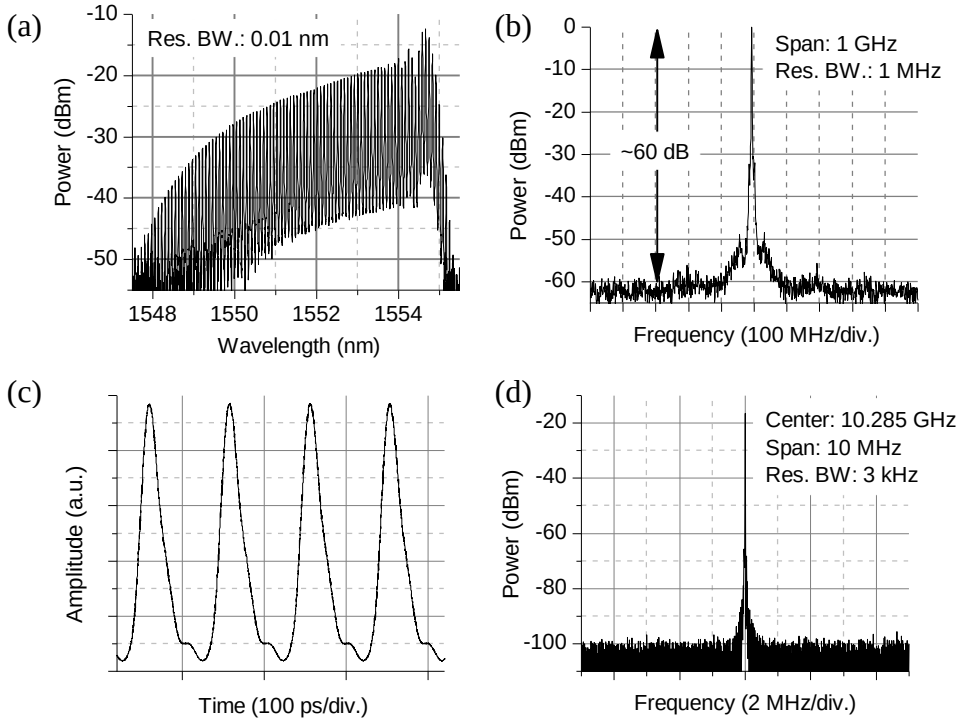

Figure 3.6 – Laser characteristics. (a) Optical spectrum, (b) High-resolution optical spectrum, (c) Photodetected pulse-train and, (d) Photodetected RF tone.

A frequency stability measurement is performed by heterodyning a relatively stable commercially available continuous wave laser with one of the mode-locked spectrum comblines and measuring the resulting radio-frequency beat-note. A spectrogram of the measurement recorded over 40 s is shown in Figure 3.7 (a). The maximum frequency deviation in this time span is ~200 kHz. An upper limit to the laser's combline linewidth can be set from these measurements as well. Figure 3.7 (b) shows a single trace of the spectrogram with and observed -3dB linewidth of < 4kHz.

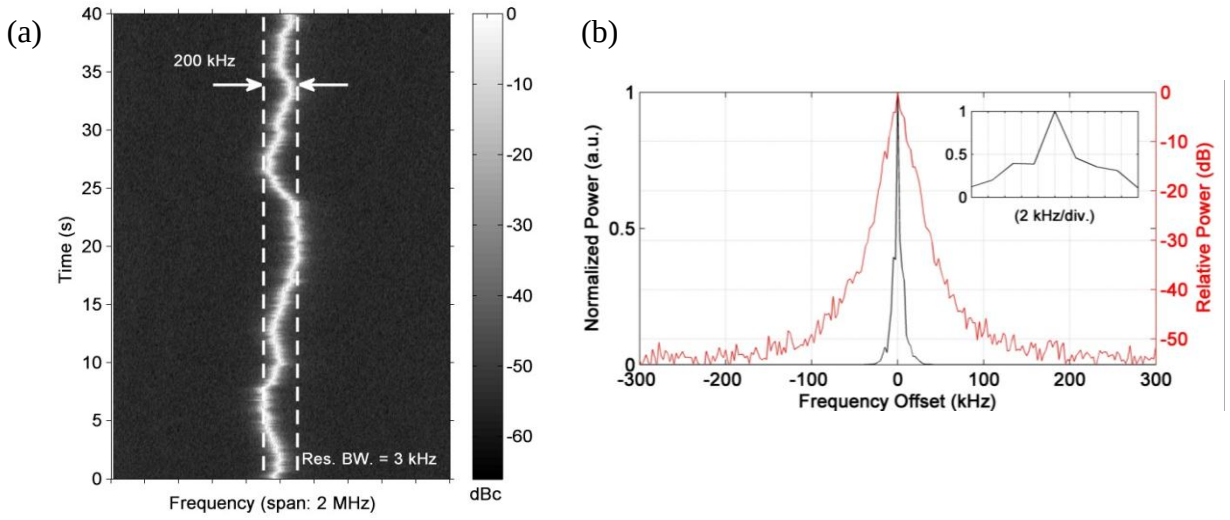

Figure 3.7 – (a) Spectrogram and, (b) a single RF trace of the heterodyne beat between a continuous-wave laser and one combline of the mode-locked laser. An upper bound to the frequency stability and the linewidth of the laser comblines can be set from these measurements.

Measuring the residual timing jitter on the pulse-train is a more challenging problem since the repetition rate of the pulse-train is twice that of the driving source. The most straightforward approach to this measurement would be to frequency divide the photodetected pulse-train using an electronic mixer with the LO driven by amplified feedback. Figure 3.8 shows the complete measurement setup including the frequency divider. The principle of operation can be easily understood if we consider a self-consistent solution with the difference frequency $f_{RF} - f_{LO} = f_{IF}$, which forces $f_{IF} = f_{LO} = \frac{1}{2} f_{RF}$. The phase shifter in the feedback loop of the frequency divider is used to match the boundary conditions of the phase of the 5.14 GHz signal that goes into the LO port of the mixer.

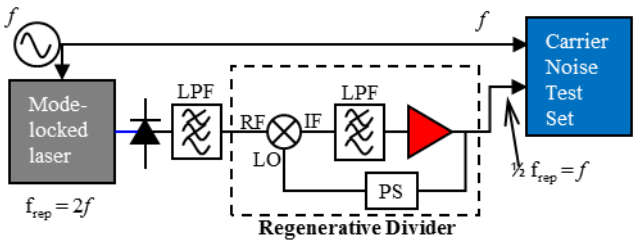

Figure 3.8 – Phase noise measurement setup using a regenerative frequency divider.

The resulting measurement is the residual jitter of both the mode-locked laser and the regenerative divider. Theory for regenerative division states that a perfect regenerative divider decreases the phase noise power spectral density (PSD) by a factor of 4 (-6 dB), which preserves the rms timing jitter of the original signal [55]. The results presented here show the noise PSD at 5.1425 GHz, and its integrated timing jitter which is that of the 10.285 GHz signal plus a small (but uncharacterized) amount added by random fluctuations in the frequency divider. Phase noise measurement results are shown in Figure 3.9. The rms timing jitter of the 10.285 GHz pulse-train is calculated to be 13 fs in the integration band from 1 Hz to 100 MHz.

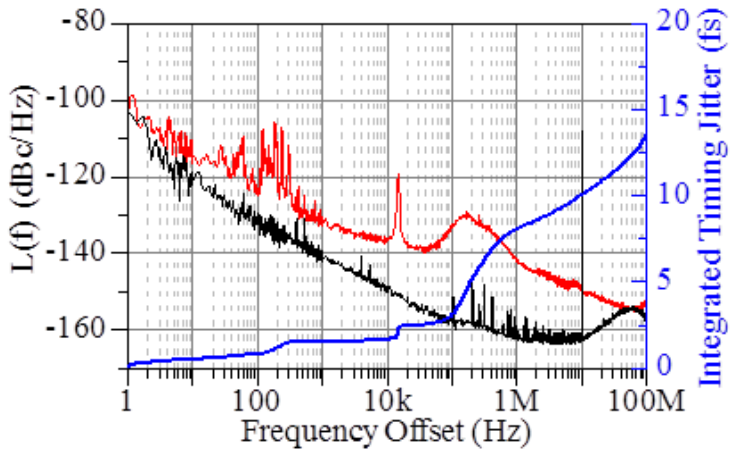

Figure 3.9 – Phase noise power spectral density of the frequency divided radio-frequency tone and integrated timing jitter. The integrated timing jitter is the same as in the 10.285 GHz signal.

3.Conclusions

In conclusion, a mode-locked laser is presented in which both mode-locking and PDH locking to an intra-cavity FPE are achieved by using a single phase modulator. The output of the laser consists of a multi-gigahertz spacing frequency comb stabilized to the transmission peaks of the FPE. The comblines exhibit a frequency instability <200 kHz over 40 seconds, which makes this laser suitable for applications in arbitrary waveform generation, coherent communications and photonic analog-to-digital conversion. A reduction of intra-cavity elements is achieved, allowing for a small footprint system. The residual timing jitter of the system is found to be 13 fs.

CHAPTER 4 : A MODE-LOCKED LASER USING A SLAB COUPLED OPTICAL WAVEGUIDE AMPLIFIER (SCOWA) AS A GAIN MEDIUM

Optical frequency combs with multi-gigahertz spacing are useful in applications such as optical arbitrary waveform generation (OAWG) [29,56,57], ultrafast signal processing [27,28], high resolution spectroscopy [23,25], and astronomical spectrograph calibration [18]. In the time domain these sources produce low-noise high-repetition-rate pulse-trains that can be used in high speed analog-to-digital conversion (ADC) [30,31,58,59], and the generation of ultra-low noise microwaves [33,34,60,61]. Low pulse-to-pulse amplitude and timing fluctuations are key to many of these applications. For example, a photonically sampled ADC at 10 GS/s requires a timing jitter smaller than 12 fs and under 0.03% of amplitude noise to operate with 10 effective bits of resolution [30].

It has been shown that low noise semiconductor-based harmonically mode-locked lasers can produce stable frequency combs with a cavity design that uses a long optical fiber cavity with a nested Fabry-Pérot etalon (FPE) [50]. In this architecture, the narrow linewidth of the individual comblines is due to the long storage time of the fiber cavity (and thus, its more stringent frequency selectivity), while the wide comb spacing is due to the spacing between the periodic transmission peaks of the intra-cavity etalon. In this chapter, we describe experiments performed to include a Slab-Coupled Optical Waveguide Amplifier (SCOWA) in a harmonically mode-locked laser with an intracavity etalon to further improve its performance. Additionally, a Pound-Drever-Hall loop is incorporated to stabilize the comb to the transmission peaks of the etalon.

This setup locks the fiber cavity fundamental frequency to a subharmonic of the etalon or, equivalently, its optical path length to an integer multiple of the round trip length of the etalon.

1.Experimental setup

The experimental setup is shown in Figure 4.1. An optical cavity with 5 MHz free spectral range (corresponding to 40 m of single mode optical fiber) is built around a Fabry-Pérot etalon with a finesse of 10^3. The laser is mode-locked via loss modulation using an intra-cavity $LiNbO_3$ Mach-Zehnder modulator driven by an ultra-low noise microwave oscillator. The modulator is driven at 10.287 GHz, to closely match the free-spectral range of the FPE. The mode-locked comb is locked to the FPE's transmission peaks through a Pound-Drever-Hall (PDH) loop, shown in the shaded box in Figure 4.1. The PDH loop consists on phase modulating the output comb at 500 MHz and reinjecting this phase-modulated comb in the FPE in an orthogonal polarization state. The reflected sidebands are photodetected and mixed with the 500 MHz tone to recover a signal that is proportional to the frequency difference between the transmission peak of the FPE and the comblines. This signal is then used to feed back into the fiber cavity length through a piezo-electric fiber stretcher. This loop essentially locks the fiber cavity fundamental frequency to a subharmonic of the FPE's free spectral range (FSR), or its optical path length to an integer multiple of the FPE's double-pass distance. A variable output coupler is used to optimize output coupling ratio. Furthermore, dispersion compensating fiber (DCF) is inserted in the cavity to make an attempt at increasing the spectral bandwidth of the output comb. Results for both the all-SMF and the dispersion compensated cavity are described in this chapter.

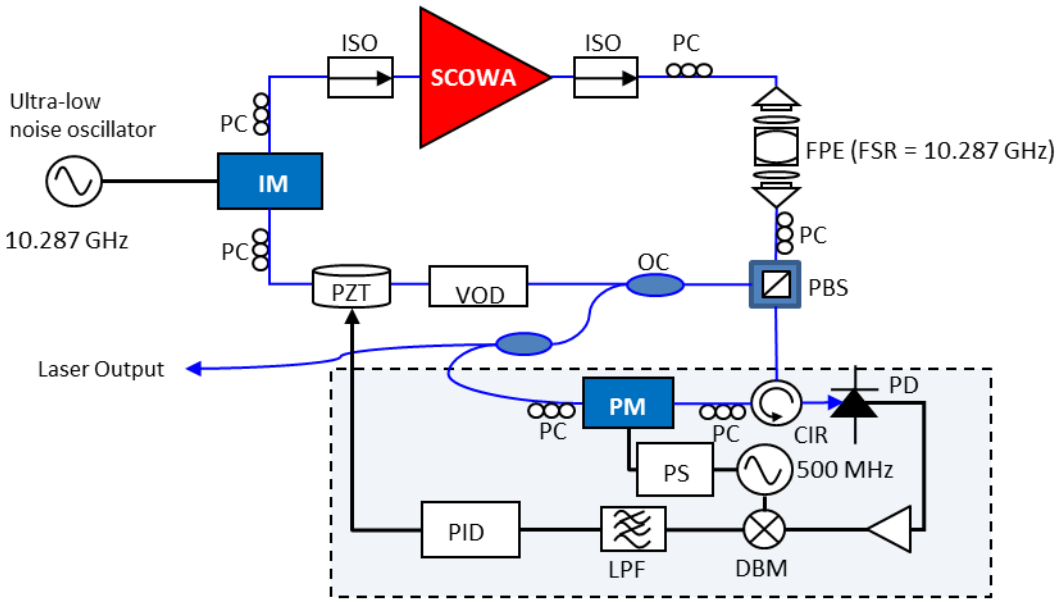

Figure 4.1. Mode-locked laser using a SCOWA and an intra-cavity Fabry-Pérot Etalon. CIR: Circulator, DBM: Double Balanced Mixer, FPE: Fabry-Perot Etalon, ISO: Isolator, LPF: Low-Pass Filter, OC: Output Coupler (Variable), PC: Polarization controller, PD: Photodetector, PID: Proportional-Integral-Differential Controller, PM: Phase Modulator, PS: Phase Shifter, PZT: Piezoelectric Transducer (Fiber Stretcher), SOA: Semiconductor Optical Amplifier (SCOWA), VOD: Variable Optical Delay

Improvements to the performance of a laser with this architecture can be achieved by increasing the quality factor of the combined cavity by either (1) increasing the fiber cavity length, which must be coupled with an increase in the FPE Finesse to be able to appropriately filter the fiber cavity modes and suppress all possible supermodes or, (2) reducing the intra-cavity losses either by careful selection of the intra-cavity elements (for example, hand-picking lower loss intensity modulators and choosing an etalon in the stable resonator region of the stability diagram which has lower insertion loss since spatial mode-matching can be easily accomplished) or by a reduction of the cavity complexity [62]. Another route to improving the oscillator quality is via the incorporation of a gain medium with higher saturation power in the cavity, which simply increases the energy stored in the cavity. In this work we have incorporated a Slab-Coupled

Optical Waveguide Amplifier (SCOWA) as a gain medium. SCOWAs have shown excellent performance with respect to high saturation power and low noise figure [63–65].

It should be noted that incorporating a SCOWA as the gain medium in this type of cavities is challenging due to the fact that SCOWAs typically have lower gain compared to commercially available devices, which considerably reduces the available loss budget. As an example, it would have been practically impossible to realize this laser using a flat-flat FPE, since the fiber-to-fiber insertion loss is typically high (~7dB). On the other hand, by using a cavity with curved mirrors, a stable resonator is achieved and the mode can be matched very closely using simple optics, which allows for coupling losses of ~1 dB or less.

The cavity dispersion is roughly matched first by inserting a low-loss patchcord of DCF that is longer than the estimated required value and then the dispersion is matched by interchanging SMF fiber lengths and optimizing the laser performance at each step until the largest bandwidth is obtained. The rationale behind this iterative procedure of varying the length of SMF instead of DCF is that given the lower absolute value of the dispersion of SMF makes it simpler to change the dispersion by a smaller amount per step.

2.Laser characterization

All SMF Cavity

The output pulse-train has an average power of 20 mW, roughly 4 times higher than previous results using commercially available devices [50]. A high visibility comb spaced by the FSR of the etalon is shown in Figure 4.2 (a). The optical bandwidth is 2 nm at -10 dB. A high resolution

measurement of a single combline is shown in Figure 4.2 (b). Notice that the optical SNR is >60 dB, limited by the noise floor of the High Resolution Spectrum Analyzer.

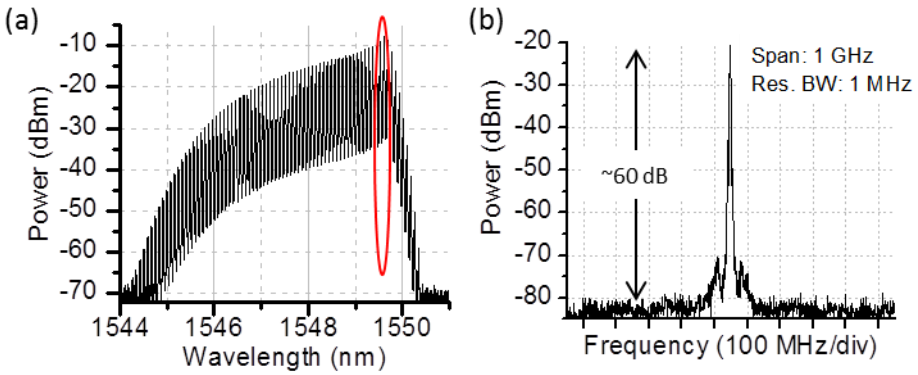

Figure 4.2 – (a) Optical spectrum and (b) High-resolution optical spectrum of a single combline.

A measurement of the optical frequency stability is presented in Figure 4.3. This measurement was done by heterodyning two similar mode-locked lasers, and then measuring the radio-frequency beat-notes, spaced by the difference of the repetition rates of the mode-locked lasers, which in this case is ~2 MHz. The maximum deviation of the combines is on the order of ~200 kHz over the span of 30 s.

Photo-detected pulse-trains and autocorrelation traces are shown in Figure 4.4. Directly from the cavity, the pulses are evidently chirped. After external compression, a close-to-transform-limited pulse can be obtained, also shown in the red trace. Notice that these pulses are still not appropriate for a photonically assisted ADC setup. This is the motivation for the addition of DCF to the optical cavity, in an attempt to increase the spectral bandwidth and, with this, the possibility of compressing the pulses to the sub-picosecond regime.

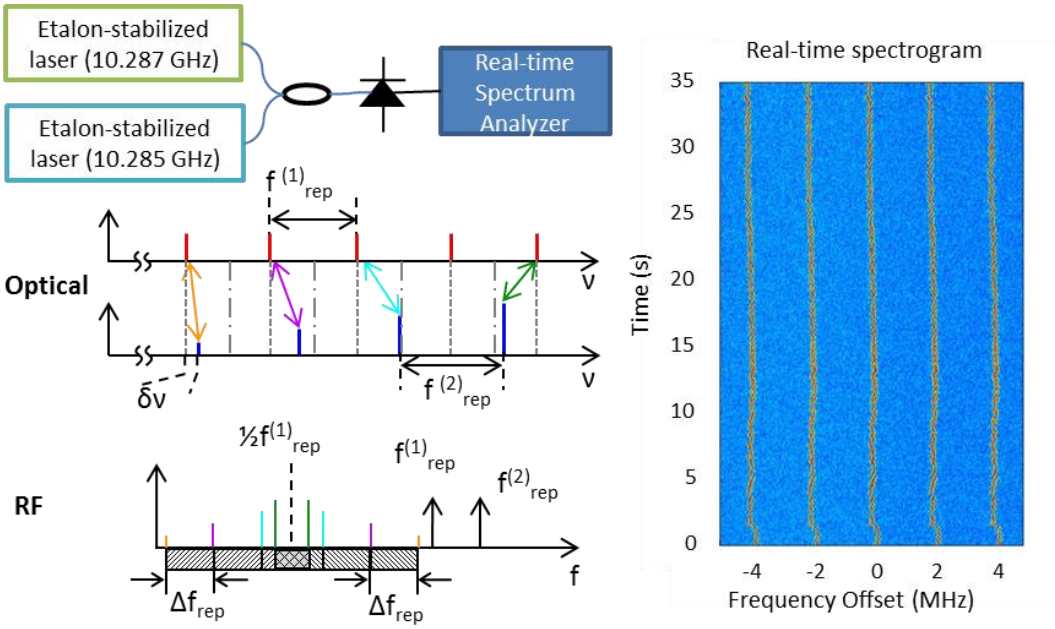

Figure 4.3 – Optical frequency stability measurement via multi-heterodyne detection with a similarly built laser. (a) Schematic of the experimental setup, (b) Conceptual description of the multi-heterodyne process and, (c) recorded real-time spectrogram.

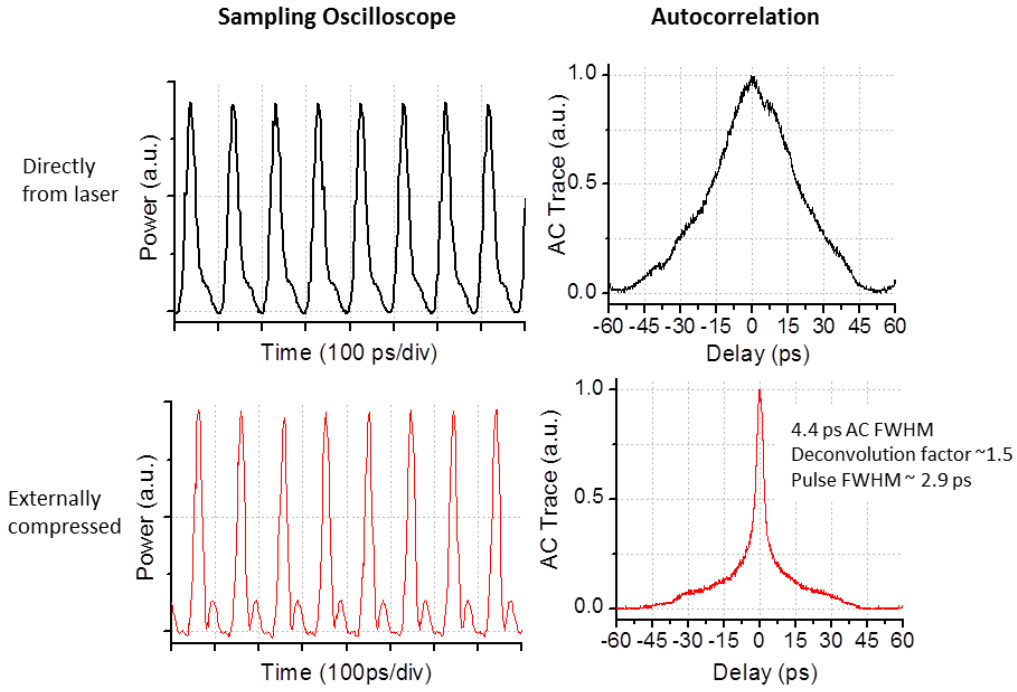

Figure 4.4 – Photodetected pulse-trains (a) directly out of the laser and (b) after external compression. (c) and (d) show the autocorrelation traces from the pulse-trains in (a) and (b) respectively.

The radio-frequency tone of the photodetected pulse-train is shown in Figure 4.5. Note that the SNR is >135 dBc/Hz.

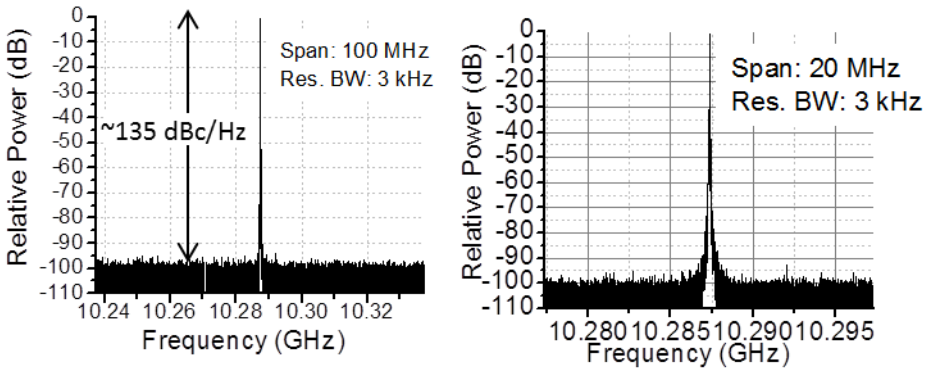

Figure 4.5 – RF tones of the photodetected pulse-trains.

The residual phase noise is measured using a carrier noise test set and it is shown in Figure 4.6 (b). Note that the white noise plateau (1 kHz to 100 kHz) is at -145 dBc/Hz. The integrated timing jitter in the band 10 Hz to 100 MHz is 1.7 fs. The noise power spectral density at 1 kHz offset represents an improvement of 5dB over ref. [50]. The phase noise PSD at 1 kHz offset (-145 dBc/Hz) matches the absolute noise of the oscillator used to mode-lock the laser, a Sapphire Loaded Crystal Oscillator. By assuming a uniform noise floor, the integrated jitter to 5.14 GHz was calculated to be 10.7 fs, meeting the requirements for a 10 GS/s photonics-assisted ADC. The amplitude noise is shown in Figure 4.6 (a). The integrated AM noise results in ~0.02% pulse-to-pulse energy fluctuations.

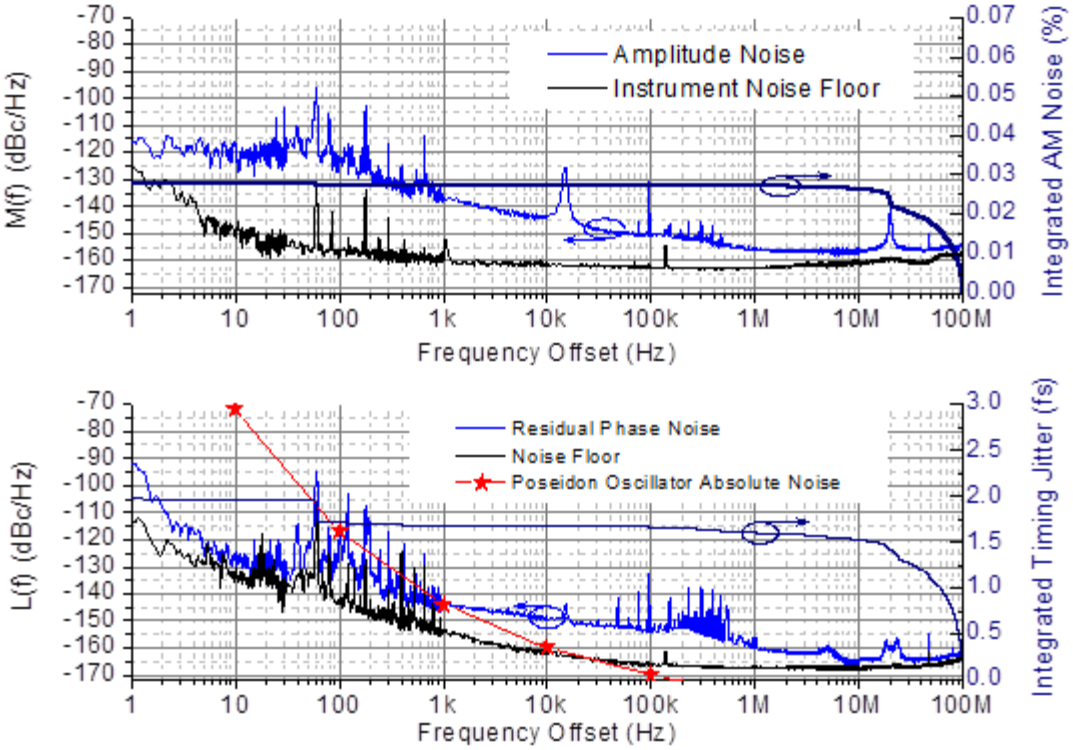

Figure 4.6 – (a) Amplitude and (b) phase noise of the 10.287 GHz pulse-train.

Dispersion compensated cavity

The incorporation of DCF in the cavity leads to an optical comb with a much broader bandwidth. Figure 4.7 (a) shows an optical spectrum with ~9.9 nm of bandwidth at -10 dB. A heterodyne beat between a stable cw laser and single comb-line is shown in Figure 4.7 (b). Shown for comparison are also two Lorentzian lineshapes, with 1 kHz (red) and 2 kHz (blue) FWHM linewidth. The output pulse-train can be externally compressed by using a dual grating compressor. Figure 4.8 shows the autocorrelation traces for the compressed pulses from the all-SMF cavity and the dispersion compensated cavity. Also shown is the calculated autocorrelation trace for the transform-limited pulse, based on the optical spectrum. Figure 4.8 (b) shows the last two traces in a 10 ps time span. The pulse-width after deconvolution is ~930 fs.

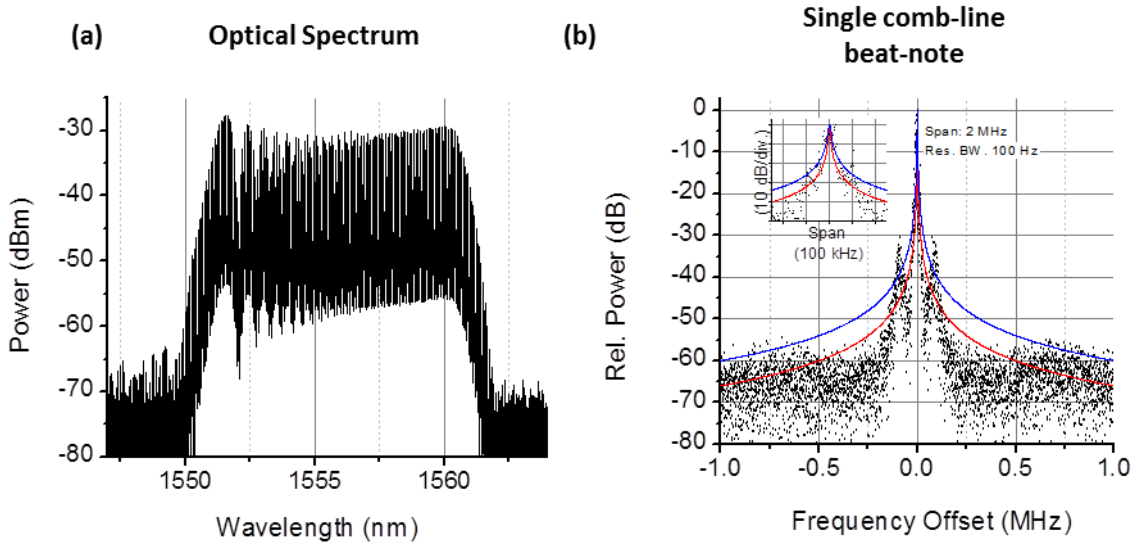

Figure 4.7. (a) Optical spectrum of a dispersion compensated laser cavity. (b) Heterodyne beat-note between a cw laser and a single comb-line. Also shown in (b) are Lorentzian lineshapes with 1 kHz and 2 kHz FWHM linewidth.

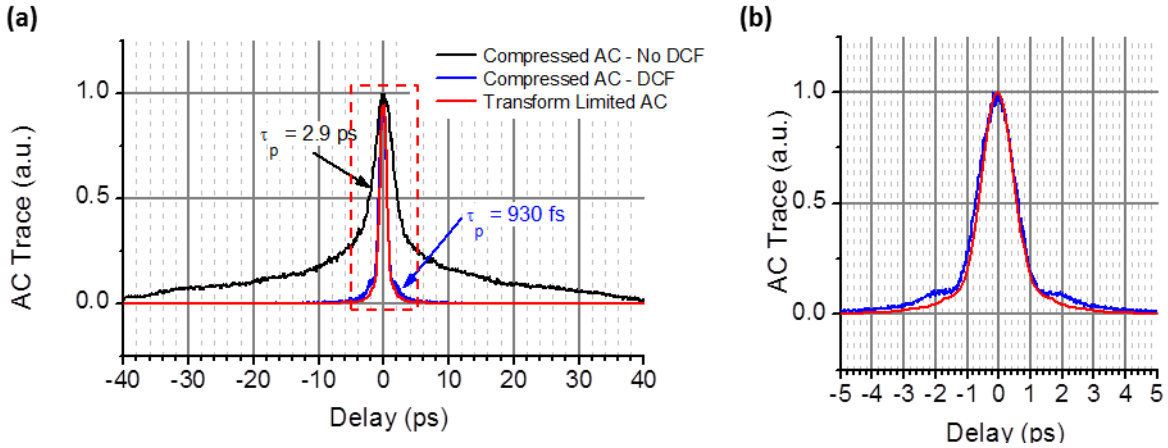

Figure 4.8. Autocorrelation traces. (a) A comparison of all the compressed autocorrelation traces in black, from all-SMF cavity, in blue from dispersion compensated cavity and in red, the calculated transform-limited pulse autocorrelation. (b) A 10 ps span plot showing only the red and blue traces.

Phase noise measurements were also performed for the dispersion compensated cavity. A summary of all the results is shown in Figure 4.9, including the absolute noise of the driving

source and the phase noise of a previously demonstrated system using a commercially-available gain medium.

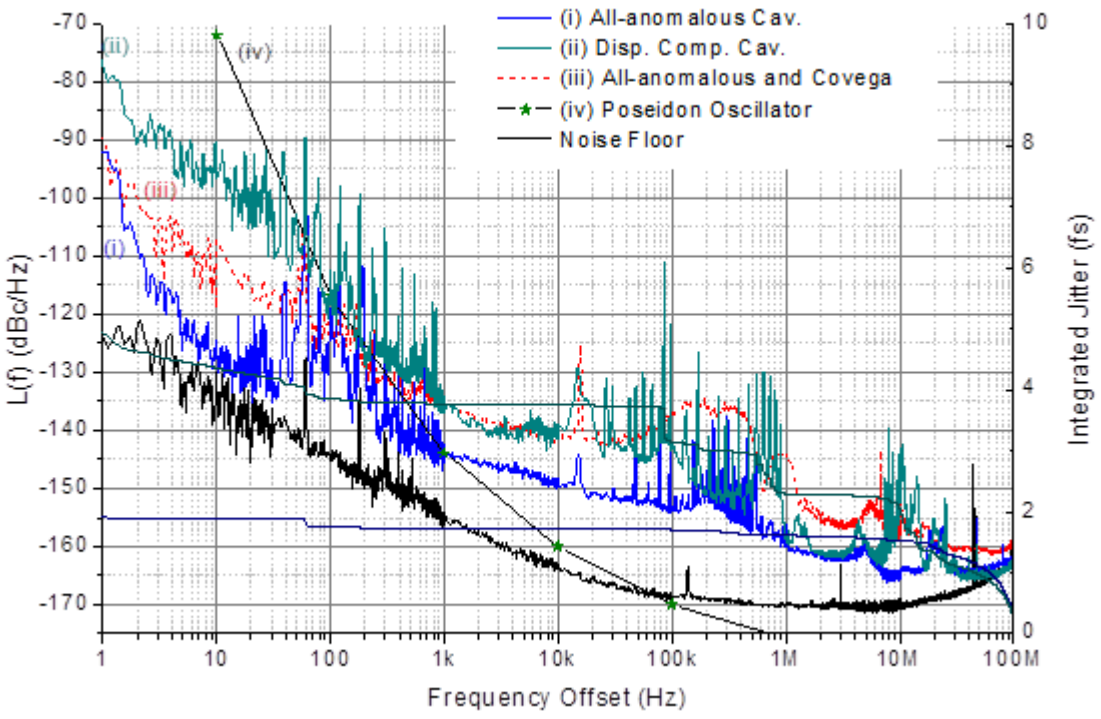

Figure 4.9. Residual phase noise measurements. The left axis shows the residual phase noise for (i) this chapter with the all-anomalous dispersion cavity and (ii) the dispersion compensated cavity; (iii) a similar laser with a commercially available gain medium [50] **and (iv) absolute noise of the mode-locking source for all cases. The noise floor shown corresponds to measurement (i), but it is comparable in the other cases. The right axis in shows the integrated timing jitter for curves (i) and (ii)**

3.Conclusions

In conclusion, we have built and characterized a comb source with 10 GHz comb-spacing using a SCOWA as a gain medium. The average optical output power is >20 mW, the optical SNR of a single comb-line is >60 dB. A broader comb can be obtained through compensation of the cavity

dispersion to ~9.9 nm. The timing jitter of the pulse-train from the all-SMF (dispersion-compensated) cavity is ~1.9 fs (4.9 fs) integrated from 1 Hz to 100 MHz and ~11 (14 fs) fs to the Nyquist frequency. The optical pulses of the dispersion compensated cavity have been shown to be compressible to <1 ps.

CHAPTER 5 : ALL-DIODE AMPLIFICATION OF 10 GHZ PULSE-TRAINS

As mentioned in previous chapters, optical frequency combs have found a myriad of applications in multiple fields and, more specifically, we have focused applications require combs with wide mode-to-mode spacing such as optical arbitrary waveform generation [29,56,66], high-sensitivity direct comb spectroscopy [67] and high-speed signal processing [28]. For different reasons, each of these applications benefits from higher power available per-combline. For example, OAWG may be performed with a setup that has high insertion loss or requires equalization of the comb components through loss modulation or the sensitivity of a spectroscopic system trying to detect trace amounts of gases at the ppb or ppt level, greatly benefits from the added SNR from higher combline power. In time domain applications such as high-speed analog-to-digital conversion, the additional power is also beneficial since the available pulse energy further separates the digitization levels and reduces the contribution of shot noise to the uncertainty of the sampled values.

In this chapter we present a master oscillator, power amplifier (MOPA) system that is entirely diode-based. At the output, the system produces a frequency comb with 10 GHz combline-to-combline spacing and a pulse-train with sub-picosecond pulse-widths. The main advantages of all-diode systems are their wall-plug efficiency, compactness and ruggedness. The amplification stage is based on a single SCOW Amplifier, operated in the stretched pulse regime. Our experiments in other regimes show that in order to obtain minimum distortions, it is ideal to operate the system amplifying chirped pulses as produced by the oscillator and subsequently

compress in a posterior stage. Spectral and temporal domain analysis of the pulse distortions is presented as well as noise characterization of the original and amplified pulse-trains.

1.Overall MOPA system

The Master Oscillator is kept as described on Chapter 4, including stabilization loops and intra-cavity dispersion compensation and a low noise Sapphire-Loaded Crystal Oscillator is used for mode-locking. The amplification stage consists of a SCOWA with lower gain and higher saturation power than the laser chip. Gain measurements with cw light input were performed and the small signal gain at 4 A of bias current is 15 dB and saturation power is ~25 dBm. The complete system is depicted in Figure 5.1. The output of the oscillator is isolated from possible reflections from connectors as well as amplified spontaneous emission from the power amplifier by placing a Faraday isolator at its output. One-tenth of the laser output is used for diagnostics, which include optical spectrum analysis, photodetection followed by RF spectral analysis and a sampling oscilloscope. The set of diagnostics connections are shown in the dashed box in Figure 5.1 and are kept as a unit and used for either the original pulse-train or the amplified pulse-train. After amplification, only one-hundredth of the output is used for the standard diagnostics and the power used in residual phase noise measurements is carefully controlled to match the power used when the same measurement is performed on the pulse-train directly from the oscillator. A dispersion stage consisting of an optimized length of SMF (depicted as D in Figure 5.1) is used to compress the pulses either before or after the amplifier.

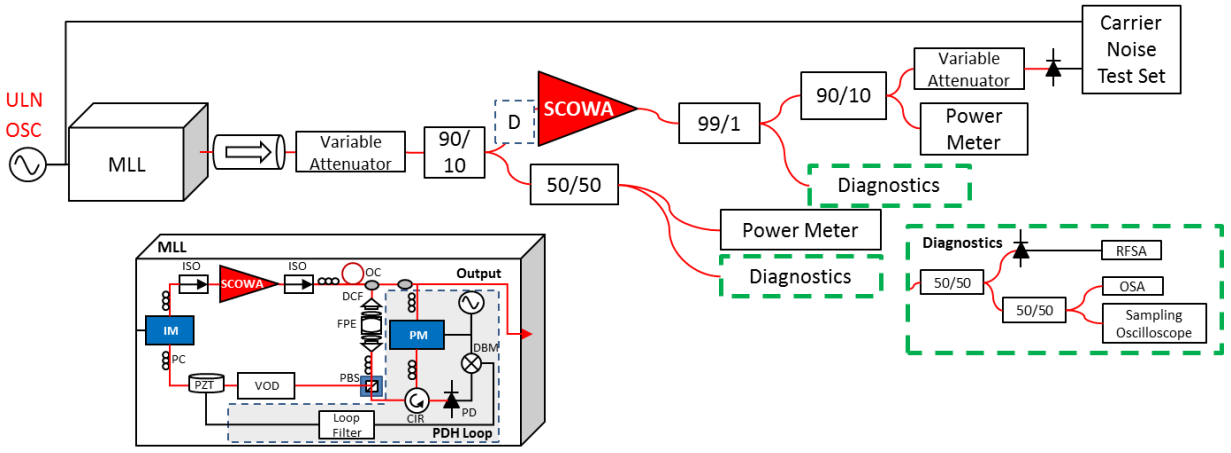

Figure 5.1. Overal MOPA system built in the laboratory. The diagnostics box shown in the dashed box contains standard diagnostics equipment and it is kept as a unit during the experiments. Phase noise measurements are performed using an attenuated beam both to protect the photodetector and to match the amount of power used from the original pulse-train. The dashed box before the amplifier is an optional dispersion stage used to compress the pulses before amplification.

2.Experimental results

Gain measurements were performed on the SCOW Amplifier using CW light from a Distributed Feedback Laser at 1550 nm, confirming the 15 dB small signal gain and the saturation power of ~25 dBm. Once in the MOPA configuration, gain measurements were performed using both the pulses directly from the laser cavity and after passing the pulses through a dispersive stage that compressed them to the sub-picosecond regime. The autocorrelation traces of the input pulses and the resulting gain measurements are shown in Figure 5.2. The gain is observed to saturate at lower average powers for the sub-picosecond pulses, reducing the saturation power by ~3 dB. Autocorrelation traces of the input pulses are shown for reference in Figure 5.2 as well. The maximum power obtained during the gain measurements is ~250 mW and the maximum observed with a 10 GHz pulse-train input is ~390 mW. The reason for this discrepancy is mainly

due to the multiple diagnostics taps used to carefully calibrate the gain measurements, which limits the amount of power available for the amplification stage.

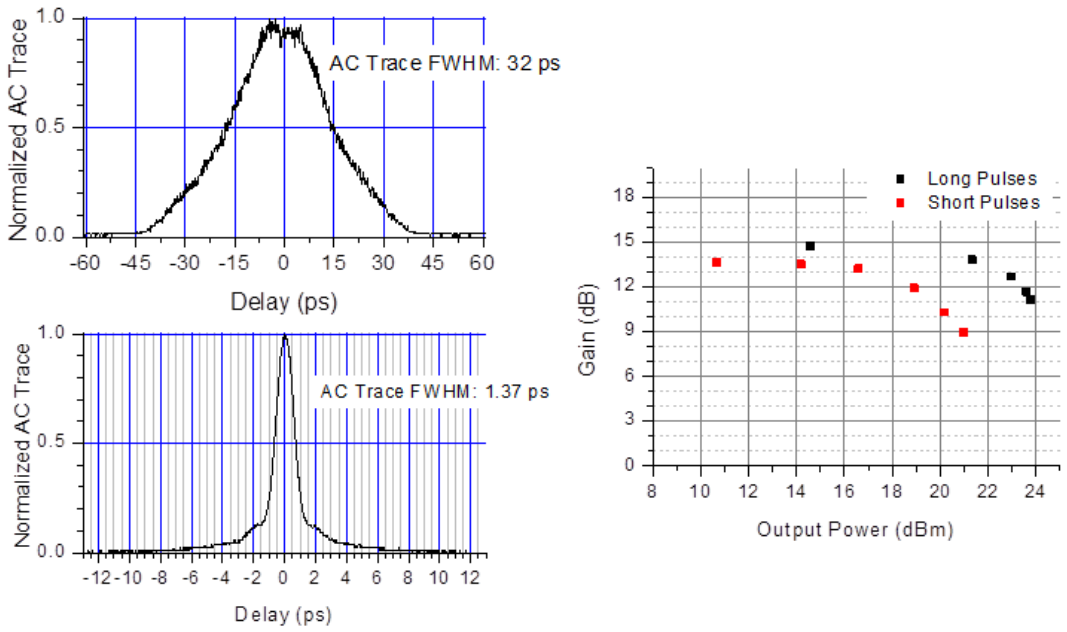

Figure 5.2. Gain measurements with pulses directly from the cavity and after compression. On the left side, autocorrelation traces of the pulses input to the amplification stage. On the right side a plot of Gain vs. Output power for the long (short) pulses in black (red).

From the gain measurements, it can be concluded that the amplifier is operating in a nonlinear regime when illuminated with short pulses; therefore the manifestation of spectral distortions is expected. To confirm this, optical spectra were recorded at different input powers to the amplifier. Figure 5.3 shows these measurements for amplification of long and short pulses. In the case of long pulses only a small red-shift is observed as the power is increased. This can be attributed to the fact that the pulses are up-chirped and therefore the red edge for the pulse sees a slightly higher gain as it passes through the amplifier. In the case of short pulses, much larger

distortions are observed as the edges of the spectrum are amplified much more significantly than the center of the spectrum generating the characteristic shape shown in Figure 5.3 (b).

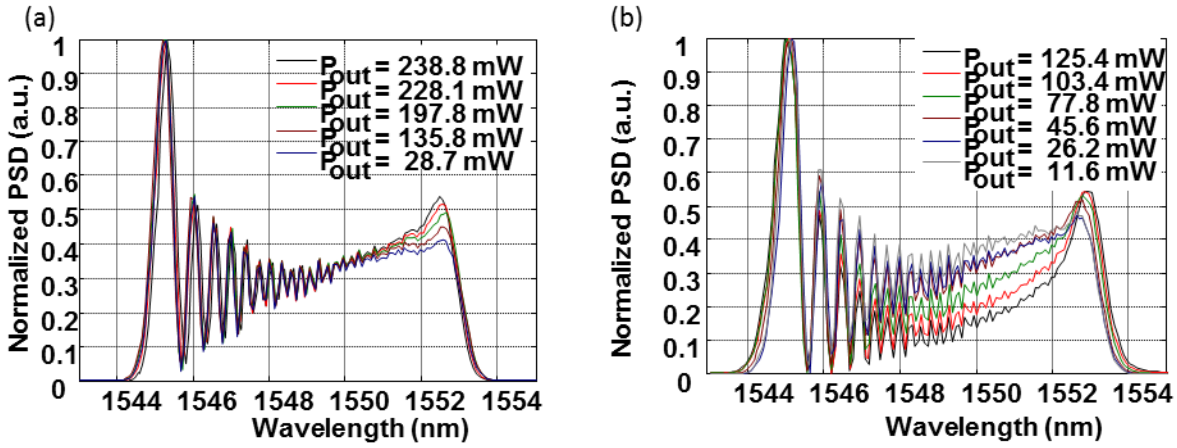

Figure 5.3. Optical spectra of the amplified pulse-trains, measured at different output powers. Amplification of (a) long and (b) short pulses.

In order to further test the distortions induced in the pulse by the saturated amplifier pulse autocorrelation measurements were also performed. Most importantly, an attempt to recompress the pulses after amplification was made, a process which should highlight higher-order phase distortions across the pulse profile, if present. The results are summarized in Figure 5.4. In Figure 5.4(a) the pulses are amplified directly as obtained from the oscillator and then compressed after amplification and on (b) the pulses are first compressed and then amplified. It should be noted that in the first case the pulses are recompressed back to the sub-picosecond regime, while in the second case the pulse autocorrelation develops 'wings' characteristic of third-order phase. Figure 5.5 shows a comparison of the autocorrelation traces of the compressed pulse-train and the amplified-and-compressed pulse-train and only minimal distortions can be observed in this measurement.

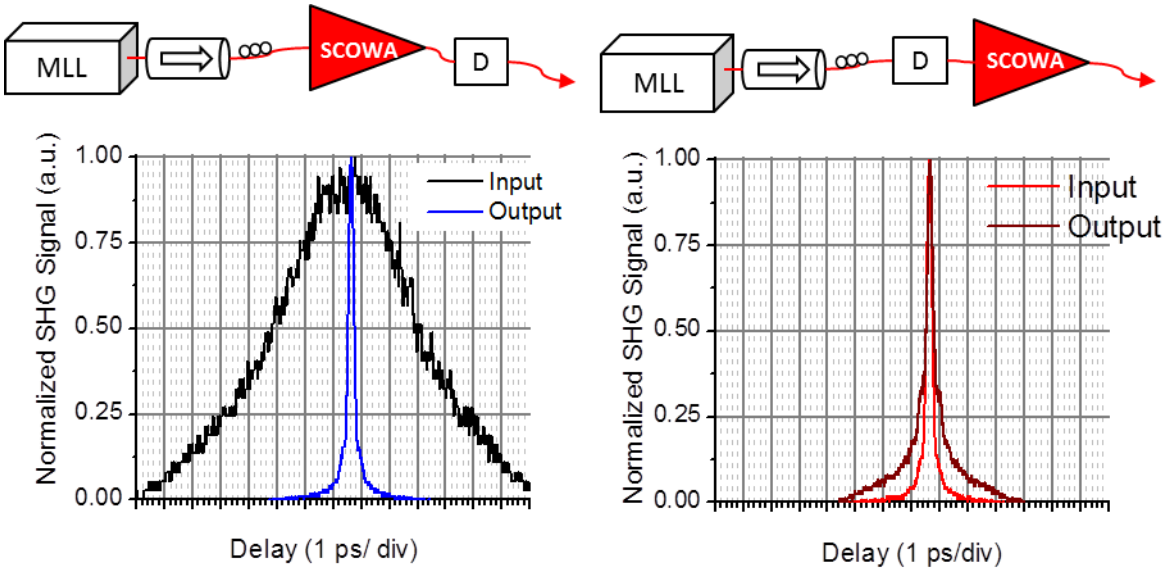

Figure 5.4. Pulse autocorrelation traces before and after amplification. (a) Amplifying pulses directly from the oscillator and subsequently compressing and (b) amplifying compressed pulses.

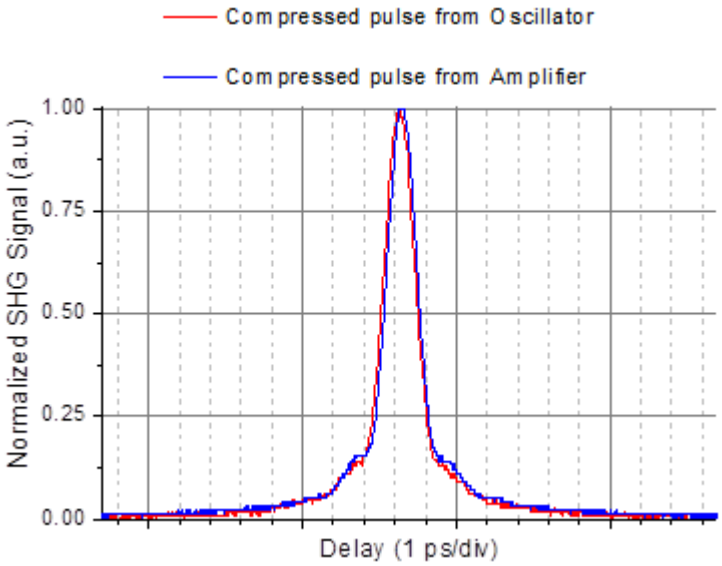

Figure 5.5. Comparison of compressed pulse autocorrelations before (red) and after (blue) amplification.

Finally, residual noise measurements were also performed on the amplified pulse-trains to quantify the noise added by the amplification stage. The results are shown in Figure 5.6 and as can be observed, no additional noise can be measured at the current stage. The technical noise is faithfully amplified together with the signal while the shot noise level is kept equal by placing equal amounts of average optical power on the photodetector.

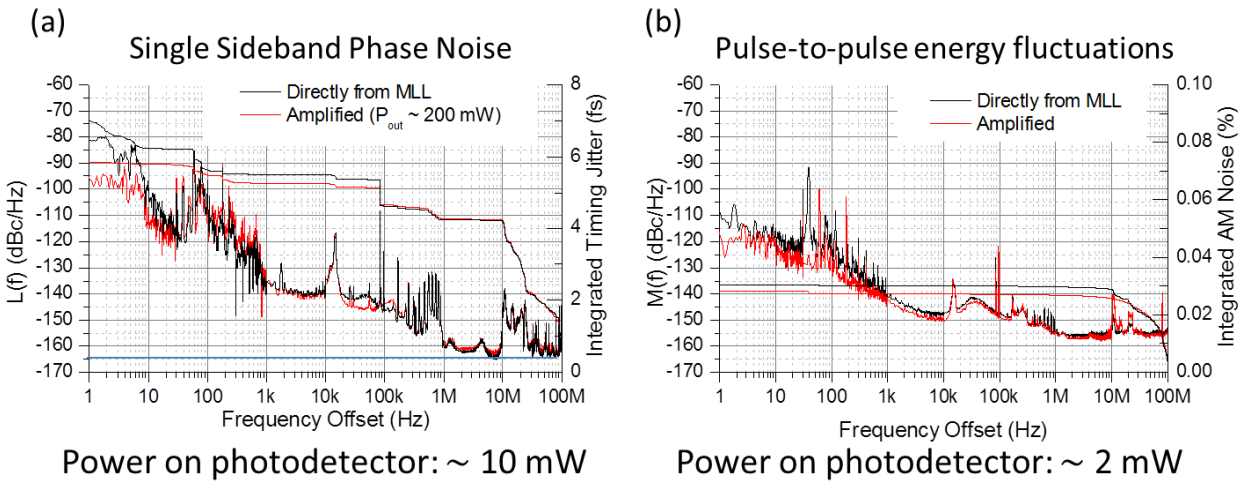

Figure 5.6 (a) Phase and (b) amplitude noise measurements for the pulse-trains before (black) and after (red) amplification

3.Conclusions

In conclusion, we have demonstrated a master oscillator and power amplifier system based entirely on diode amplifiers which produces >250 mW of average optical power (maximum observed 390 mW) in a 10 GHz optical frequency comb. The amplification can be performed with minimal distortions if the amplification stage is fed with chirped pulses as produced by the oscillator and the output of the amplification stage has been compressed to the sub-picosecond

regime. These systems can potentially find applications on optics-assisted sampling for analog to digital converters, optical arbitrary waveform generation and multi-heterodyne spectroscopy to name a few.

CHAPTER 6 : FREQUENCY STABILITY OF A MODE-LOCKED LASER WITH A 10,000 FINESSE FABRY-PEROT ETALON

The central element in the type of comb sources presented in this dissertation (as well as in refs. [35,50]) is the inclusion of a high-finesse optical cavity, coupled to a long fiber ring cavity. The reason behind the inclusion of such high-finesse filter is the suppression of the interleaved cavity modes to accomplish a laser that operates as a comb source at 10 GHz. Besides this, the Fabry-Pérot Etalon (FPE) accomplishes at least three more purposes inside the cavity. The first one is the elimination of the so-called supermode noise spurs, which present themselves as noise that is periodic with the fundamental frequency of the cavity a known detrimental effect of harmonic mode-locking. The second effect is that this cavity is able to filter out broadband spontaneous emission from the gain medium and the last one is that the FPE becomes a frequency reference for the comb-lines. In this chapter, a new laser system using a 10,000 Finesse etalon is constructed and characterized. This FPE is held in a vacuum chamber whose temperature is controlled in order to achieve an improvement on the absolute frequency stability of the comb. Also, an attempt is made at measuring the suppression of out-of-band ASE by placing several output couplers around the optical cavity and making spectral measurements with both a system with a 1,000 Finesse etalon and a 10,000 Finesse etalons.

1.Experimental setup

The experimental setup of the laser used in this chapter is shown in Figure 6.1 and it is very similar to previous implementations of the system, so details about the general laser architecture

are omitted in this chapter and the reader is referred to previous chapters and refs. [35,50] where details about the operation and performance of previously demonstrated sources can be found. In brief, the laser is mode-locked via loss modulation by driving the intensity modulator (IM) at a rate equal to the free-spectral range (FSR) of the FPE. The cavity length is actively stabilized by using a multi-combline Pound-Drever-Hall (PDH) stabilization scheme, shown in the dashed box in Figure 6.1. Note that multiple taps have been placed around the cavity which are used to characterize the evolution of the pulses as they travel around the cavity. The optical cavity is comprised mostly of single mode fiber (~20m) and a short section of dispersion compensating fiber (~2m), yielding a ~9 MHz cavity, which is then mode-locked at a harmonic close to the ~1,130th, to closely match the FSR of the FPE. Contrary to previous experience, it was found that it was quite challenging to mode-lock the laser before the dispersion compensation was in place. We currently attribute this to a walk-off between the cold fiber cavity modes and the modes of the FPE.

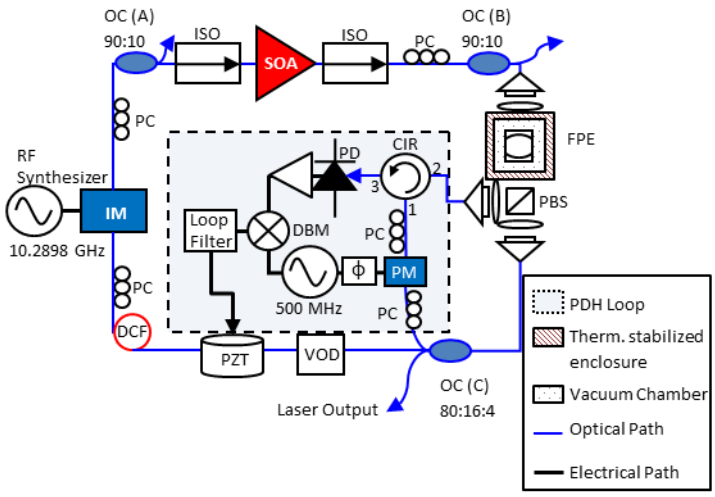

Figure 6.1. Schematic of the mode-locked laser utilized in this experiment. CIR: Circulator, DBM: Double Balanced Mixer, DCF: Dispersion Compensating Fiber, FPE: Fabry-Pérot Etalon, IM: Intensity Modulator, ISO: isolator, OC: output coupler, PC: Polarization controller, PD: Photodetector, PBS: Polarizing Beam Splitter, PM: Electro-optic Phase Modulator, PZT: Piezoelectric Fiber Stretcher, SOA: Semiconductor Optical Amplifier, VOD: Variable Optical Delay. The PBS used to multiplex the error signal is a bulk component. The FPE is kept in a vacuum and temperature stabilized enclosure.

2. Experimental results

Characterization data of the laser is shown in Figure 6.2. Figure 6.2 (a) shows two optical spectra taken from the port B, immediately after the SOA (red line) and from port C, after the light has passed through the FPE (black line). It is evident from the plot that background ASE is significantly filtered by the cavity. In the plot shown ASE is suppressed to below the noise-floor of the instrument. Further measurements were performed and are compared to a mode-locked laser with a 1,000 Finesse etalon in the next section. Figure 6.2 (b) shows two autocorrelation traces after the pulses have been passed through 20 m and 90 m of SMF. The smooth curve (blue) is a calculation of the transform-limited autocorrelation using the measured optical spectrum. The full-width at half-maximum (FWHM) of the measured autocorrelation after 90 m

of SMF is ~4 ps while the calculated transform-limited autocorrelation is ~3 ps FWHM. The calculated deconvolution factor is 1.43, yielding a deconvolved pulse-width of ~2.8 ps. The pulse compression was not optimized for these measurements.

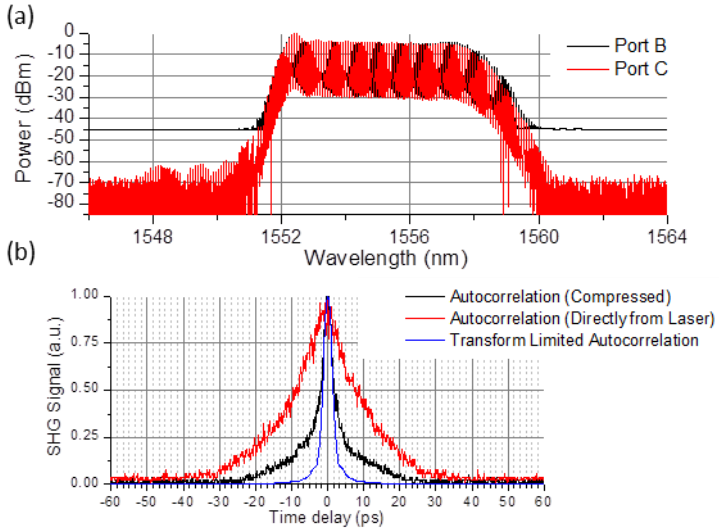

Figure 6.2. Characterization of the laser output. (a) Optical Spectrum measured at port B (black) and port C (red). (b) Autocorrelation traces with the pulses passing through ~20 m of SMF and ~90 m of SMF. In blue, the calculated transform-limited autocorrelation.

While it has been shown that timing jitter in a mode-locked laser scales inversely with the cavity Q as well as the intra-cavity power [68], the stability of the optical frequency of the comb-lines is anchored to the length of the FPE's spacer via the PDH stabilization setup. Despite the fact that previous lasers were constructed with FPEs with ultra-low expansion (ULE) quartz spacers, environmental fluctuations were still observed to couple in and cause a measurable change in the optical frequency of the lasing modes (see refs. [35,50,62], Figure 3.7 and Figure 4.3). In this laser we have improved on the performance of our previous lasers both by using a higher finesse Etalon and by placing it in a temperature stabilized vacuum chamber. And, as expected, the

obtained comb is much more robust against environmental fluctuations. In previous measurements, we were also limited by the fact that the laser used for the comparison was free-running [50,62]. To improve our measurement method, we have used a fully stabilized frequency comb as reference. The experimental setup for the measurement is shown in Figure 6.3. The reference comb is a commercially-available (Menlo Systems), fiber-based mode-locked laser in which both f_{rep} and f_{ceo} are stabilized to a microwave reference. The repetition rates are detuned from an exact harmonic in order to generate a multi-heterodyne spectrum, which is subsequently filtered and analyzed in a real-time spectrum analyzer. The only drawback of this setup is that the reference comb has a relatively broad comb line-width, in the order of 100 kHz.

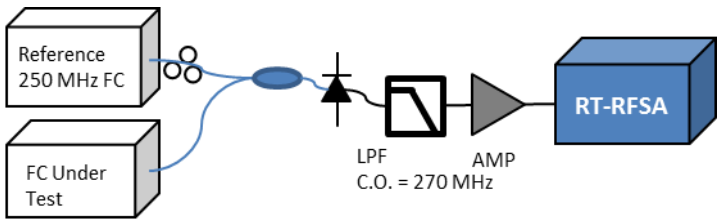

Figure 6.3. Multi-heterodyne experimental setup. RT-RFSA: real time Spectrum Analyzer.

The beating of two frequency combs produces a multi-heterodyne spectrum, which allows us to track the frequency of multiple (14 in this case, but this is not limited by the method) beat-notes simultaneously using a real-time radiofrequency spectrum analyzer to record the spectrogram which is then analyzed for frequency deviations. The repetition rate of the reference source is stabilized to 250.955 MHz and the source under test is mode-locked at the FSR of the FPE, 10.2898 GHz. Therefore, the effective repetition rate detuning $\Delta = f_{rep}^{1} - 41 \times f_{rep}^{2} = 645\text{kHz}$. A single trace of such multi-heterodyne spectrum is shown in Figure 6.4. These spectra were continuously recorded for ~6 min on one measurement day (Dec/13/2012) and for ~12 min the

next day (Dec/14/2012). The centroid frequency of the beat-note is calculated for each of the peaks as well as a standard deviation. The standard deviation confirms the expected line-width of the beat-note.

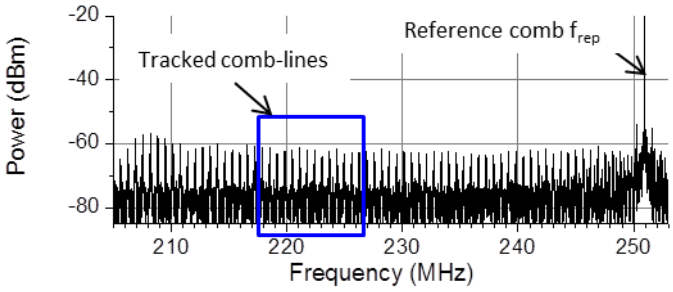

Figure 6.4. Single trace of the multi-heterodyne spectrum. Each comb-line is clearly resolved. The following measurements are the result of tracking the 14 comb-lines in the blue box.

The measurement of the optical frequency stability of the comb yields a maximum deviation of <100 kHz in over 12 minutes of continuous operation. This measurement only sets an upper limit to the deviations because despite the fact that the reference comb has excellent frequency stability, the linewidth of its comb-lines suffers and we are unable to detect deviations that are smaller than said line-width. The beat-note centroids are shown in Figure 6.5. Notice that there are two sets of traces taken 20.5 hours apart and the average frequency of the comb-lines only changes by an amount smaller than the line-width of the reference source. The PDH lock had to be restarted multiple times between the two measurements and it is possible that the observed shift is due to locking at a different position in the FPE's resonance. Regardless of the origin of the shift, it is important to note that this shift is at least one order of magnitude smaller than the environmentally caused deviations in previous implementations of our comb-sources.

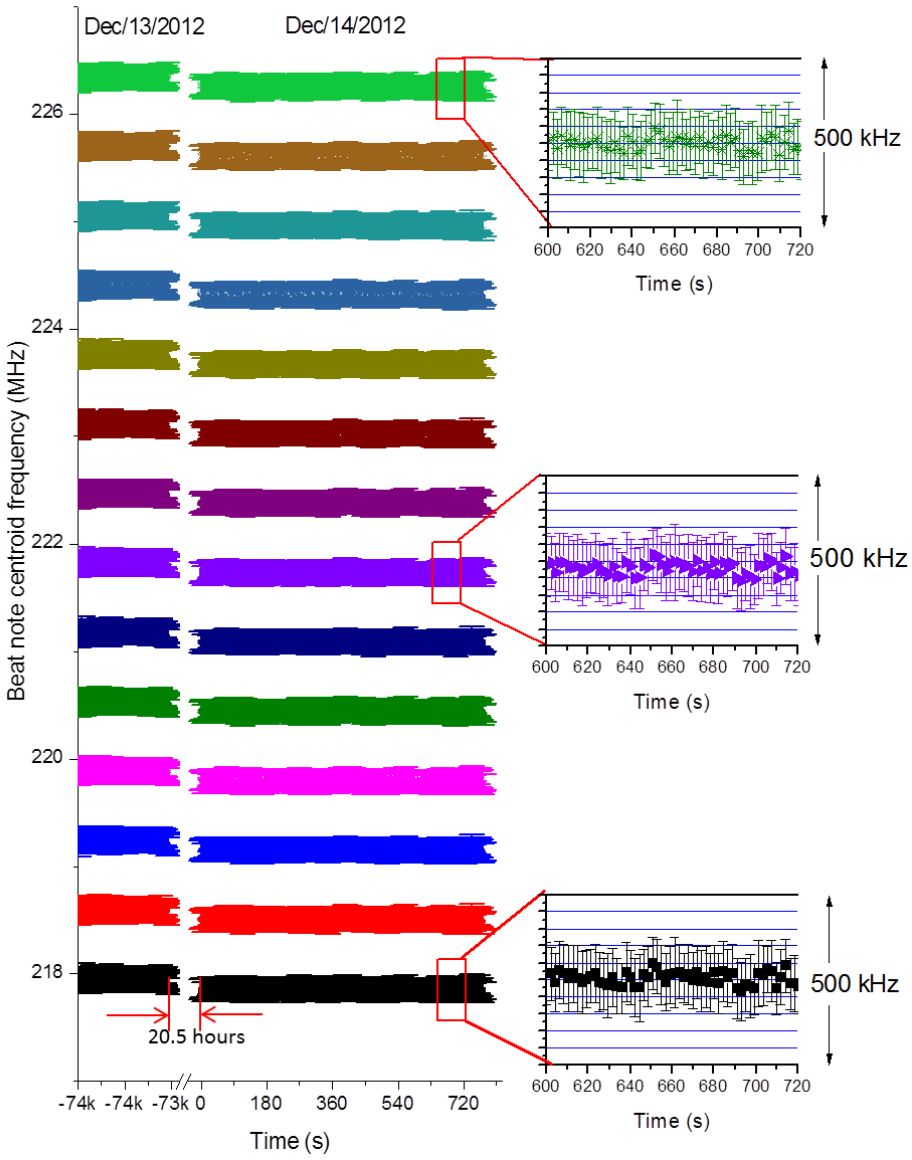

Figure 6.5. Long term tracking of the comb-line frequency. The data on the left side was taken on Dec-13-2012 and on the right on Dec-14-2012. The laser operated continuously but it had to be relocked several times in between. The plotted data shows the beat-note centroid and the error bars correspond to ±1σ. Notice that the centroid always remains within a 100 kHz window and the average value of σ is ~80 kHz.

The beat-note centroid position has been statistically analyzed as well for the 12-minute long dataset. As shown in Figure 6.6, the maximum observed deviation over the full time span is

always under 100 kHz (< 90 kHz, with the exception of an anomalous data-point in the second beat-note) and twice the standard deviation is <40 kHz.

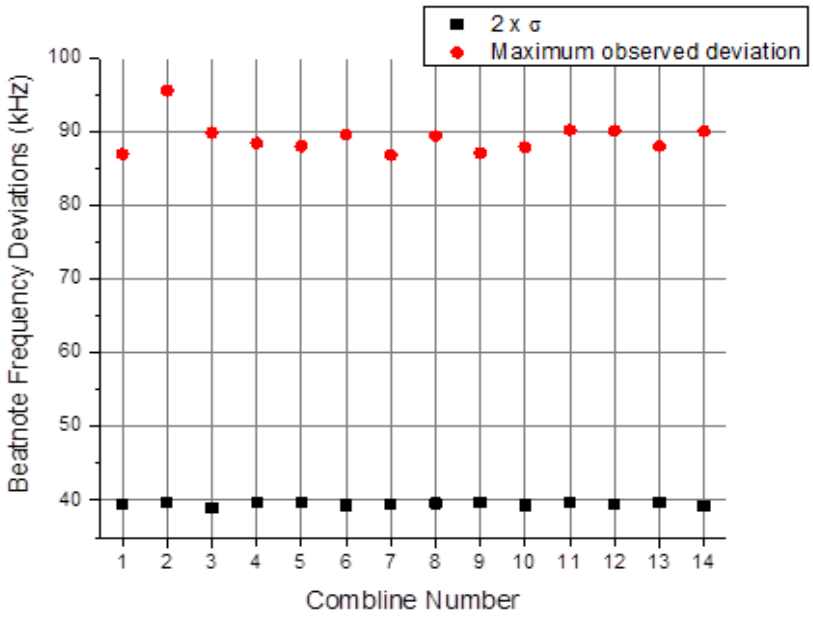

Figure 6.6. Statistics of the beat-note centroid positions. 2xσ is plotted in black squares and the maximum observed deviation over 12 minutes in red circles. Notice that even the maximum observed deviations are within one beat-note line-width.

3. Amplified spontaneous emission suppression as a function of filter Finesse

Another one of the functionalities that the FPE performs in the cavity is the suppression of broadband amplified spontaneous emission from the amplifier. A simple mathematical analysis of the transfer function of the FPE shows that the expected suppression is inversely proportional to the Finesse of the FPE. Measurements of this suppression were performed on a mode-locked laser with a 1,000 Finesse etalon and then with a 10,000 Finesse etalon by recording the optical spectra in a coupler before and after the FPE. The fiber cavities contained the exact same

elements besides the 2 m DCF patchcord that was included in the laser with the 10,000 Finesse FPE. The results are shown in Figure 6.7, where we can see that the suppression of broadband ASE outside the lasing spectrum is ~27 dB in the 1,000 Finesse etalon case and ~37 dB in the 10,000 Finesse etalon.

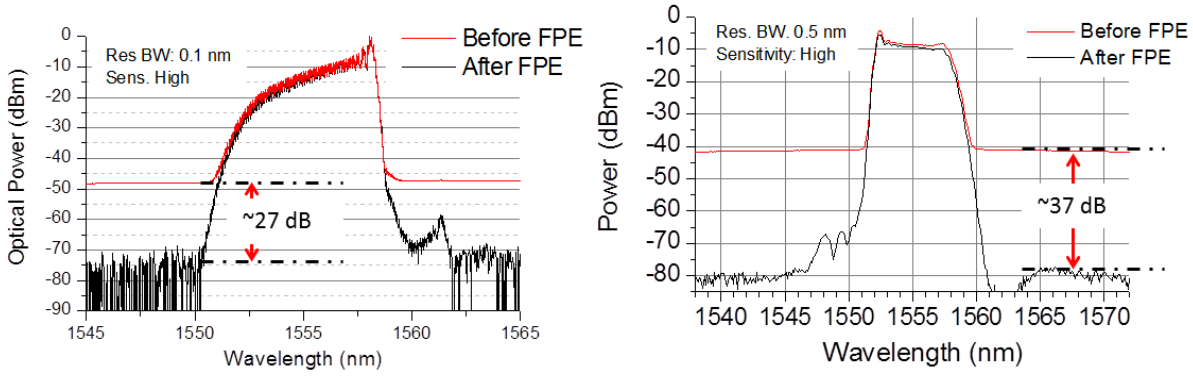

Figure 6.7. Broadband ASE suppression for a mode-locked laser using (a) 1,000 Finesse and (b) 10,000 Finesse etalons.

4. Conclusions

In conclusion, we have demonstrated an etalon-stabilized, harmonically mode-locked semiconductor laser with an optical frequency instability <100 kHz that lasts for continuous operation times longer than 12 min. The optical spectrum consists of a frequency comb with 10.2898 GHz comb-line to comb-line spacing. Such sources could find applications in astronomical spectrograph calibration, optical arbitrary waveform generation, signal processing among other fields. Future improvements to the system include increasing the cavity length to mode-lock at a much higher harmonic (around 10,000) while keeping the dispersion compensation.

CHAPTER 7 : APPLICATION OF FREQUENCY COMBS IN MULTI-HETERODYNE MEASUREMENTS. PART I: THEORY

Since its invention, the optical frequency comb [1,3,69], has been applied to several fields such as time and frequency metrology [4,70,71], length metrology [20], optical arbitrary waveform generation [27,28,56,66,72,73], and high precision spectroscopy [23]. All of these applications benefit from the fact that the frequency comb consists of a large set of coherent local oscillators with uniform frequency spacing. These oscillators can then probe the resonances of a molecular or atomic system in spectroscopic measurements, and become the Fourier basis whose amplitudes and phases are controlled for arbitrary waveform generation or provide the link between the optical frequency of a single combline and the microwave frequencies represented by the combline spacing in optical clocks.

Sampling electric fields directly at optical frequencies is practically an impossible task given the fact that the center frequency of the oscillation is well beyond the capabilities of electronic sampling devices. Notwithstanding, most optical signals contain information only within a small bandwidth (i.e., they are bandlimited). Heterodyning a high-frequency but bandlimited signal with a coherent oscillator produces an exact copy of the bandlimited signal centered at a frequency corresponding to the frequency difference between the coherent oscillator and the signal under test. This low-frequency copy can then be sampled by electronic means. This principle can be applied to optical signals, that is, a narrowband optical signal can be heterodyned with a continuous wave (CW) laser and sampled at the beat frequency. If the signal

is distributed over periodically spaced portions of spectrum, it can be heterodyned with a set of coherent oscillators with different frequency spacing to generate a series of beat notes in the RF domain that can then be sampled. Heterodyne techniques are useful because both amplitude and phase information are retained in the process. Some of the requirements for the local oscillators are frequency stability and a fixed phase relation between them, both of which are typically met by frequency comb sources.

Multiheterodyne detection with optical frequency combs was first proposed in [22] and has been implemented in a coherent configuration where two combs that share an optical reference are mixed and from the mixing products the effect of a medium on the signal comb can be deduced [23,74,75]. The mutual coherence of these combs makes possible the accumulation of signal over extended periods of time, beyond the coherence time of individual comblines.

In our experiments, we utilize a frequency comb as a set of local oscillators to downconvert and sample periodic optical signals. The optical signals that are being sampled are not coherent with the local oscillator, which is a realistic approximation to measuring unknown optical signals as is the case in the spectral characterization of rapidly tunable CW lasers [76], mode-locked laser systems, and arbitrarily shaped optical waveforms. The most evident limitations are that the waveforms must have an underlying periodicity and that the lack of mutual coherence sets a limit on the maximum time over which signal can be accumulated. Three types of experiments are presented, wherein different types of sources are sampled: 1) pulses from an independent optical frequency comb source; 2) phase-modulated, CW light; and 3) periodically filtered, incoherent white light. In the first two experiments, the repetition rates are extremely detuned, by more than

a multiple of the repetition rate of the lower repetition rate source and, therefore, the downconversion is performed using only a subset of the available comblines. An effective repetition rate detuning is introduced to accurately describe these experiments. In the third case, photocurrent interferometry of signals detected with time delays between them is performed to demonstrate the fidelity of the measurement.

This chapter is organized as follows. In the next section a conceptual description of the experiments is presented by considering the sources to have infinitely narrow (represented by Dirac delta functions) frequency components. Following this section, a more rigorous treatment of the signals is presented and the analysis extended to random signals with bandlimited spectral content. The experimental results are left for the next chapter where our experiments will be described in detail.

1.Conceptual description

Equivalent time and frequency domain pictures can be drawn to explain the phenomena at hand. A conceptual form of the experimental setup is shown in Fig. 1, where one of the sources is an optical frequency comb and the other is the source under test. For this description, we shall assume that the source under test is a frequency comb with narrow components whose amplitudes and phases are unknown. This assumption is valid as long as the observation time does not exceed the coherence time, which can be on the order of hundreds of microseconds to milliseconds for free-running, narrow-linewidth lasers [50], while cavity stabilized lasers have reached the sub-hertz linewidth regime [77–79], allowing for second-long observation times.

In reference to Figure 7.1 (a), the source under test is depicted to have a repetition rate that is equal to four times that of the LO plus a small additional detuning. This additional detuning determines the rate at which the waveforms "walk" through each other, generating a slowly varying interference pattern which repeats itself at a rate equal to the difference between the repetition rate of the source under test and the closest harmonic of the repetition rate of the LO.

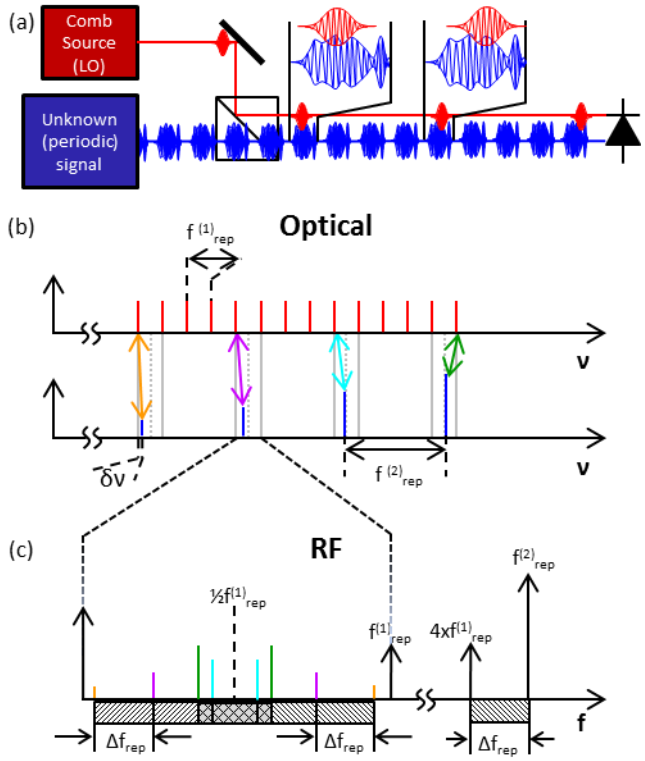

Figure 7.1 – Conceptual picture of the multiheterodyne detection with a large repetition rate detuning. (a) Time domain depiction of the process. Notice the pulse walk-off between the LO and the signal under test. (b) Frequency domain picture in the optical domain and (c) the photodetected spectrum of the superposition of the two optical combs. The highest frequency combline pair (green) illustrates the aliasing effect. This is illustrated by the shaded areas underneath the frequency axis as well, with an overlapping region. Also note the difference in scales between the optical and RF frequency axes.

From the frequency domain picture [see Figure 7.1 (b) and (c)], it can be readily seen that the RF beat notes will appear at the frequency difference between each pair of comblines. The effective repetition rate detuning determines the rate at which the comblines from each source walk-off from each other, thus determining the beat-note spacing in the RF domain. It should be noted that for large detuning or a large interacting bandwidth, the beat notes may get to the point where the next closest combline is not to the lower frequency side but to the higher frequency side. When this occurs, a different set of beat notes with the same spacing but at an overall offset will appear within the region of interest, generating a signal with a slower overall periodicity (aliased). To avoid this problem the following limit must be satisfied:

$$N \times \left|\Delta f_{rep}\right| + \delta\nu < \frac{1}{2} f_{rep}^{(1)} \tag{7.1}$$

In this expression, N is the number of interacting comblines, $\Delta f_{rep} = f_{rep}^{(2)} - Round\left(f_{rep}^{(2)}/f_{rep}^{(1)}\right) \times f_{rep}^{(1)}$ is the effective repetition rate detuning, $f_{rep}^{(2)}$ is the larger of the two repetition rates, and $\delta\nu$ is the frequency difference between the two closest comblines. From (7.1), we can see that there is a tradeoff between the maximum repetition rate detuning and the available interacting bandwidth. The frequency difference of the two closest comblines also affects the maximum usable bandwidth and, in some cases, it can be tuned to a convenient value by changing the carrier-envelope offset frequency of the reference comb. For example, assume $f_{rep}^{(1)} = 1\text{GHz}$ and $f_{rep}^{(2)} = 4.01\ \text{GHz}$, then $\left\lfloor f_{rep}^{(2)}/f_{rep}^{(1)} \right\rfloor = 4$ and the beat-note spacing $\Delta f_{rep} = 4.01\ \text{GHz} - 4 \times 1\ \text{GHz} = 10\ \text{MHz}$. A maximum of 50 beat notes can be

observed within the band from dc to $f_{rep}^{(1)}/2 = 500$ MHz, which limits the optical bandwidth that can be used before aliasing effects appear to a maximum of 200 GHz.

The equivalent time domain picture is that of a sampling gate that has variable delay with respect to the periodic signal under test, given by the pulse walk-off. The relative position of the pulses/waveforms comes back to its original position after a time equal to $1/\Delta f_{rep}$, which in turn gives rise to the beat-note spacing in the RF domain.

It is important to note that this is a linear technique and, consequently, the interacting quantities are the electric fields. The resulting waveforms arise from electric field interference, which, if the local oscillator is properly characterized, gives a snapshot of the periodic signal under test, including the carrier under the envelope.

This process achieves two independent forms of spectral conversion: 1) it downconverts the carrier frequency from the optical domain to the RF domain; and 2) it compresses the spectrum by reducing the "empty" spaces in between comblines from the original repetition rate to the new sampled rate, given by the repetition rate detuning. The downconversion factor can be defined as the carrier optical frequency divided by the carrier microwave frequency and the compression factor as the ratio of the original repetition rate to the sampled repetition rate.

As the repetition rate detuning is reduced, the generated waveforms have a longer periodicity. This detuning must evidently reach a point where the periodicity is longer than the coherence of the sources. In the frequency domain, this can be thought of as an overlap between finite-linewidth components (as opposed to the ideal delta-like components described so far) when the

spectral compression is carried beyond the linewidth of individual comblines. A more detailed analysis of the signals obtained from finite linewidth signals is presented in the next section, but it must be stated that a lower limit to the repetition rate detuning can be written as:

$$\Delta f_{rep} > \Delta \nu_{LW} \qquad (7.2)$$

where $\Delta\nu_{LW}$ is a parameter that represents the linewidth of the individual comblines and its definition may vary depending on the particular application.

2.Heterodyne detection of bandlimited white light and periodically filtered white light

When the source under test is a bandlimited white light source, the corresponding electric fields can be represented through a Fourier expansion whose frequency component pacing depends inversely on the observation time. A classical analysis for the correlations between two delayed copies of a white light signal is developed by Hanbury Brown and Twiss [80]. In this paper, a heterodyne version of the derivation is presented for a single combline and the conclusions can be extended to the multi-combline beating by superposing individual solutions as long as the condition in (7.2) is fulfilled.

An advantage of using heterodyne detection to downconvert a white light spectrum is that the resulting photocurrent interferometry has extremely high resolution, limited only by the available RF spectrum analyzers. As a comparison, a typical grating based optical spectrum analyzer can resolve fringes with a resolution on the order of 1 GHz, while a RF spectrum analyzer could

potentially resolve spectral fringes with spacing smaller than 1 Hz. The power spectral density of the white light spectrum then becomes the ultimate limitation in the detectability of the fringes.

A few assumptions must be stated first: 1) The white light is considered band-limited; 2) the local oscillator is assumed to be coherent (i.e., a delta-like function); and 3) the frequency difference between the local oscillator and the closest nonzero frequency component of the white light is larger than the white light bandwidth. This allows us to treat the white light homodyne beats independently from the heterodyne beats. The assumptions are not extremely constraining, provided careful filtering.

A random but bandlimited optical field is considered in this derivation. In general, the spectrum of a bandlimited signal may consist of a finite number of sparsely located finite bandwidth peaks. If such a random electric field is observed for a finite time τ, then it can be represented by a Fourier series in the following form:

$$E_{ASE}(t) = 2 \sum_{n=n_0}^{n=n_0+N} |q_n| \cos\left[\frac{2\pi n}{\tau} t + \phi_n\right] \quad (7.3)$$

where the coefficients q_n are related to the integrated optical power in the *n*th frequency bin and are nonzero only for a finite frequency range, $\nu_{min} < \frac{n}{\tau} < \nu_{max}$. ϕ_n are the phases of the frequency components and are assumed to be uniformly distributed over the range [0,2π]. As shown in the analysis in [80], the photocurrent generated by such a field is given by

$$i(t) = \mathcal{R}\langle P_{ASE}\rangle + 2\mathcal{R} \sum_{n>m} \sqrt{P_n}\sqrt{P_m} \times \cos\left[\frac{2\pi}{\tau}(m-n)t + (\phi_m - \phi_n)\right] \quad (7.4)$$

where $\mathcal{R}$ is the photodetector responsivity, $\langle P_{ASE} \rangle$ is the average power contained in the signal and P_n and P_m are the average powers contained in the *n*th and *m*th frequency bins, respectively. The photocurrent fluctuations represented by the second term in (7.4) average zero, but, nonetheless, they can be shown to be correlated to the signals detected at a time delay Δt_A. The case that is of interest to us in this work is a heterodyne version of this experiment. The total electric field obtained by adding a CW carrier to a random signal like the one in (7.3) is given by:

$$E_{tot}(t) = 2A\cos[2\pi\nu_L t + \phi_c] + 2\sum_n \cos\left[\frac{2\pi n}{\tau}t + \phi_n\right] \quad (7.5)$$

The photodetected signal has four main components: the two terms in (7.4) plus an additional average power due to the local oscillator and a heterodyne term. As long as care is taken to keep the frequency difference between the local oscillator and the center of the white light's spectrum larger than the white light bandwidth, the heterodyne term can be filtered and observed independently in the RF domain. The voltage across a resistor R_L of the heterodyne part of the photodetected signal is given by

$$V^{(1)}(t) = \mathcal{R}R_L\sqrt{P_L}\sum_n \sqrt{P_n} \times \cos\left[2\pi\left(\frac{n}{\tau} - \nu_L\right)t + (\phi_n - \phi_L)\right] \quad (7.6)$$

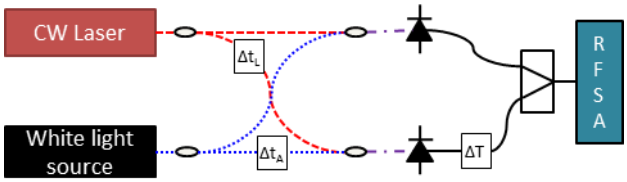

Figure 7.2 – Conceptual experimental setup for white light photocurrent interferometry.

After including delays at different positions (see Fig. 9) at the second photodetector, the voltage is

$$V^{(2)}(t) = \mathcal{R}R_L\sqrt{P_L}\sum_n \sqrt{P_n} \times \cos\left[2\pi\left(\frac{n}{\tau} - \nu_L\right)t + (\phi_n - \phi_L) + \frac{2\pi n}{\tau}\Delta t_A - 2\pi\nu_L\Delta t_L\right] \quad (7.7)$$

Note that phase delays in the optical paths (Δt_A and Δt_L) change the phase of the photodetected spectrum directly. If we add the signals $V^{(1)}$ and $V^{(2)}$ in an RF coupler as shown in Figure 7.2, the interference pattern will have a fringe spacing related to the accumulated delay between the white light paths, but the fringe position will be extremely sensitive to small path changes in the order of the wavelength of light, due to the phase factor $\left(\frac{2\pi n}{\tau}\Delta t_A - 2\pi\nu_L\Delta t_L\right)$. The expression for the spectral interference is given by:

$$\left|\mathcal{F}\left\{\frac{1}{2}\left(V^{(1)}(t) + V^{(2)}(t)\right)\right\}\right| = \cos\left[2\pi\left(\frac{n}{\tau} - \nu_L\right)\Delta T + \frac{2\pi n}{\tau}\Delta t_A - 2\pi\nu_L\Delta t_L\right] \times \widetilde{V^{(1)}}\left(\frac{n}{\tau} - \nu_L\right) \quad (7.8)$$

where $\widetilde{V^{(1)}}(n/\tau - \nu_L)$ is the Fourier transform of the signal in a single channel. Notice that n/τ and ν_L are optical frequencies. As a consequence, while the *periodicity* of the interference pattern

changes with the difference frequency $\left(\frac{n}{\tau} - \nu_L\right)$, its *phase* (or the absolute position of the fringes in the RF spectrum) is sensitive to delays (Δt_A) smaller than the wavelength of light.

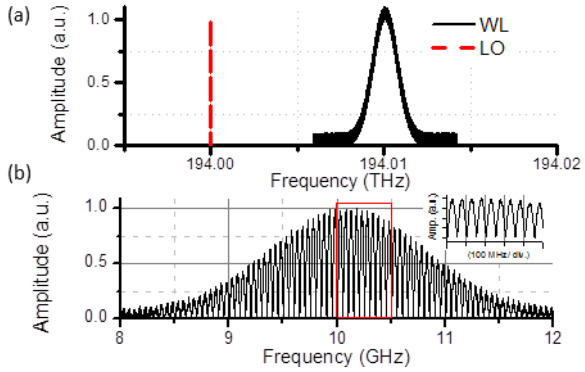

Figure 7.3 – Simulation results. (a) Optical spectra. (b) Photocurrent interference for a fixed 20 ns delay

Figure 7.3 shows a numerical calculation of the interference in the RF spectral domain of a heterodyne white light signal. Figure 7.3 (a) shows the optical spectra, with the CW laser in red and the white light modeled with a random amplitude variations on top of a Gaussian spectrum and uniformly distributed random spectral phases. The interference pattern for a path delay ($\Delta t_A = 20$ ns) is shown in Figure 7.3 (b).

CHAPTER 8 : APPLICATION OF FREQUENCY COMBS IN MULTI-HETERODYNE MEASUREMENTS. PART II: EXPERIMENTAL RESULTS

The experiments presented cover various cases for which multiheterodyning an unknown, periodic, optical signal with a frequency comb is useful as a means to downconvert and sample the electric fields. Although all the experiments are conceptually very similar, in practice, they represent a broad set of cases. For this reason, the metrics for evaluation of the performance of the experimental setups are chosen specifically for each of the experiments. In some cases, the availability of different diagnostic tools also determines the type of analysis that can be performed.

This chapter is organized as follows: the first section deals with pairs of optical frequency comb sources generated from mode-locked lasers, the second section deals with a mode-locked laser comb which samples phase modulated continuous wave light and the third section includes experiments done with periodically filtered white light.

1.Mode-locked pulses

In the first experiment, an erbium-doped fiber passively mode-locked laser source is used as a local oscillator to sample the electric field from a semiconductor-based harmonically mode-locked laser, locked to an intracavity Fabry–Pérot etalon (FPE) [35]. The repetition rates of the

lasers are ~250 MHz and ~10.24 GHz, respectively. The detuning is extremely large and only the beat notes from the 250 MHz spaced comblines that are nearest to the 10 GHz spaced comblines are used in the measurement, yielding an effective repetition rate detuning of ~600 kHz, which is calculated by comparing the 41st harmonic of the fiber laser with the fundamental of the 10.24 GHz comb source. This is equivalent to sampling one out of every forty-one 10.24 GHz repetition rate pulses on each cycle.

Optical and RF spectra of the results are shown in Figure 8.1. An effort was made in this experiment to make the detuning large enough to almost fill the available RF bandwidth (1/2 of 250 MHz) for one copy of the spectrum. The absolute position of the downconverted comb can also be controlled by varying the carrier-envelope offset frequency of the 250 MHz comb. A smaller span of the RF measurement shows clearly resolved beat notes in Figure 8.1 (c). The interacting bandwidth is essentially the optical bandwidth of the semiconductor mode-locked laser which is ~2.12 THz, that is, more than 200 comblines. The downconversion factor $\left(\nu_{opt}/f_{RF}\right)$ is on the order of 3×10^6, and the compression factor $\left(\Delta\nu_{opt}/\Delta f_{RF}\right)$ is $\sim 17 \times 10^3$.

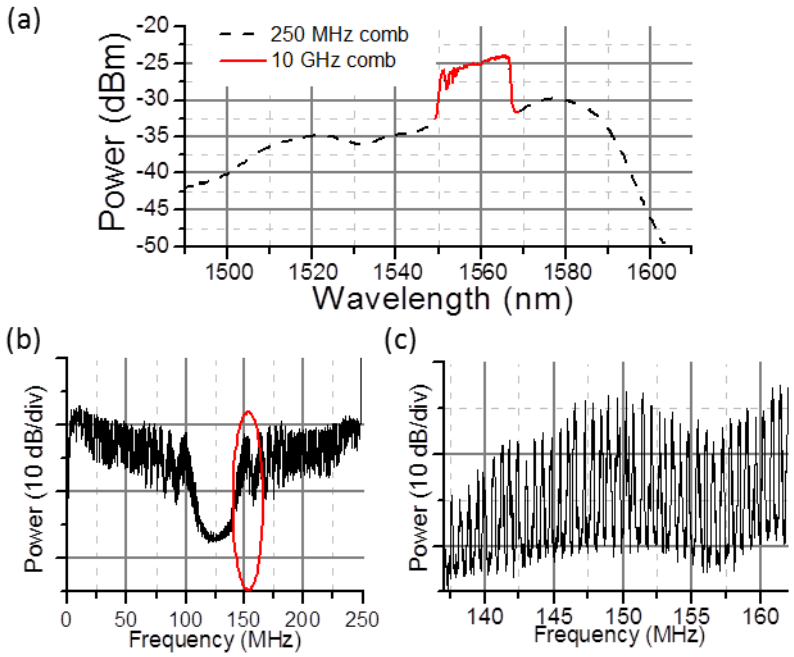

Figure 8.1 – (a) Optical spectra of the mode-locked comb sources. (b) Photodetected RF spectrum. (c) Smaller span of the RF spectrum.

In order to test whether the spectral phase information is preserved, the photodetected signal is low pass filtered (ideally with a filter that cuts off everything above 125 MHz, but in this case, the oscilloscope bandwidth was limited to 80 MHz) and the resulting waveform is sampled with an electrical oscilloscope. The semiconductor laser's pulses are then passed through different amounts of dispersion (~100 m of standard single-mode fiber with $D \approx 17\,\mathrm{ps/(nm \cdot km)}$ and a few meters of dispersion compensating fiber with $D \approx -170\,\mathrm{ps/(nm \cdot km)}$). The results are shown in Figure 8.2, where it can be observed that as the pulse chirp, and hence, the spectral phase of the optical signal is varied, the chirp and pulse duration of the RF signal varies accordingly.

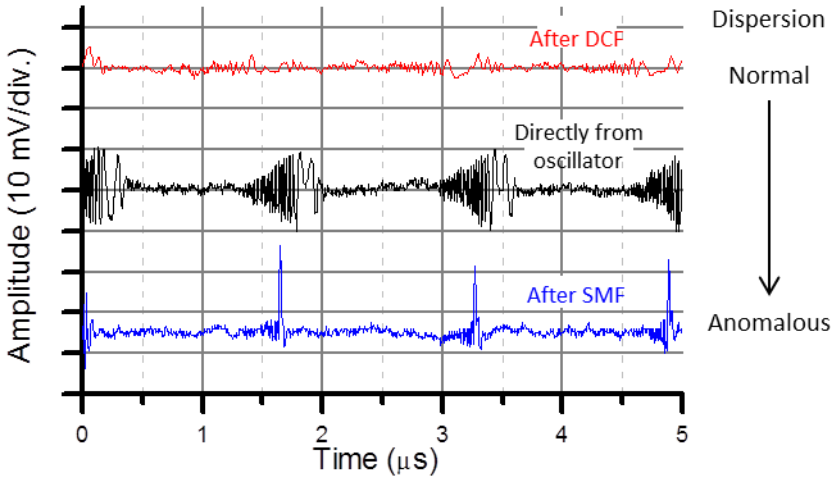

Figure 8.2 – Time domain RF waveforms after downconversion as the 10.24 GHz mode-locked comb experiences different amounts of dispersion.

It is interesting to note in Figure 8.2 that the sampled pulses coming straight from the laser cavity are chirped as expected from a semiconductor laser. The sharp rise in the front edge and the long tail are evidence of residual third-order phase. The RF carrier in these waveforms is chirped, mirroring the optical carrier of the mode-locked pulses, because the sampled RF waveforms contain information about the instantaneous optical frequency.

The measurements presented in this section give a good picture of the spectral intensity of the target comb. The spectral phase is preserved relative to the reference comb. As long as the reference comb has a flat phase profile over the interacting bandwidth, the sampled waveform represents the target E-field accurately. Knowledge of the absolute frequency of each combline would require resolving the combline number ambiguity from the reference comb. That is, knowledge of the absolute frequency of the reference comb combined with the ability to trace the unique RF beats of each combline pair yields the absolute frequency of the target comblines. This issue has also been addressed in [76] for the measurement of the absolute frequency of CW

lasers by using two reference frequency combs with detuned repetition rates. The sensitivity of our measurement is ultimately limited by the length of time over which a signal can be accumulated due to the lack of coherence between the target and reference combs.

2.Phase modulated light

Another particular case of interest is that of phase-modulated CW light. In fact, recent work [76] has been done in the measurement of the absolute frequency of rapidly tuned CW lasers. The lack of intensity fluctuations and the fact that there is only a slow change in optical frequency make it an interesting case to test some of the limits of the technique. For example, the small number of interacting comblines reduces the number of free parameters and it is therefore easier to fully characterize the experimental data by fitting the measured waveform to an expected theoretical waveform.

The experimental setup is shown in Figure 8.3. As in the previous experiment, the same commercially available, 250 MHz, erbium-fiber frequency comb is used as a local oscillator in this experiment to downconvert the comb generated by phase modulation at 10.006 31 GHz of CW light from a commercially available CW laser. In order to fully recover the comb parameters, it is desirable to obtain a high-fidelity sampled electrical waveform. Besides careful low-pass filtering to avoid higher frequency components to leak into the sampling device, good suppression of the 250 MHz tone from intracomb beatings is imperative to best use the available resolution of the sampling device. For this reason, an interferometric carrier suppression arm is

used, as shown in Figure 8.3. Additional filtering can be done in the digital domain after the data have been recorded.

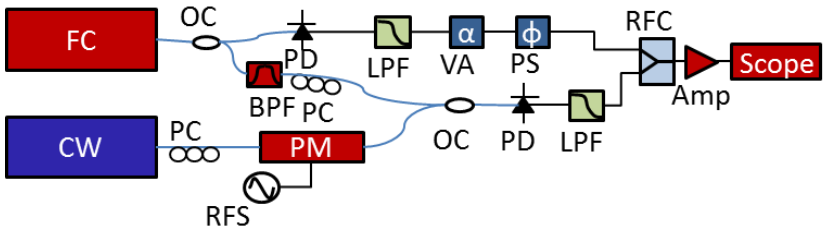

Figure 8.3 – Experimental setup. Amp: amplifier, BPF: bandpass filter, FC: frequency comb, CW: CW laser, LPF: low-pass filter, OC: optical coupler, PC: polarization controller, PD: photodetector, PM: phase modulator, PS: phase shifter, RFC: RF coupler, RFS: RF synthesizer, VA: variable attenuator.

The optical spectrum of both sources is shown in Figure 8.4 (a), and the photodetected RF spectrum is shown in Figure 8.4 (b). Notice the difference in the 250 MHz carrier suppression through the interferometric filtering.

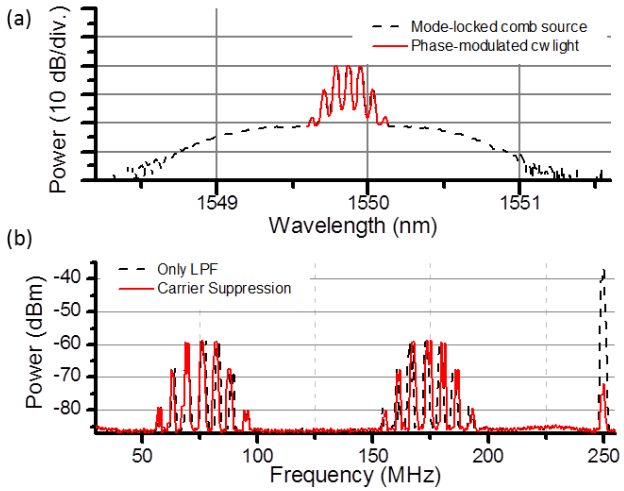

Figure 8.4 – (a) Optical spectra of the phase-modulated CW light and the reference comb. (b) Photodetected RF spectrum.

A real-time high bandwidth oscilloscope was used to record waveforms obtained from the multiheterodyne beat notes. After filtering the beat notes between 70 and 120 MHz, an example

of the obtained waveform is shown in Figure 8.5 with a time-shifted (by ~1/2 of a period of the repetition rate detuning) version of the same waveform shown in the red trace to show that the frequency modulation of the waveform can be observed by inspection. The repetition rate detuning was ~6.31 MHz and ~1262 cycles of this waveform were recorded in this case. The time axes can be conveniently normalized to the repetition period. A Fourier transform of the entire dataset is shown in Figure 8.5 (b). Figure 8.5 (c) shows the Fourier transform of a 1.6μs segment of the sampled signal. The spectral phase of this fast Fourier transform (FFT) is available as well and shown in the figure after removing a constant offset and a linear trend. Notice the expected π phase shift between the ±1 comblines. The spectral phase can only be recovered from a shorter time segment of the signal because of the free-running nature of the target comb with respect to the LO comb, which causes the signal to add incoherently for time spans longer than the inverse of the linewidth of the comb teeth.

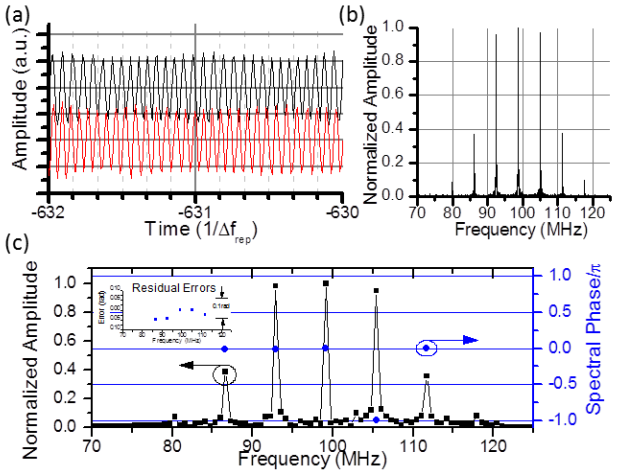

Figure 8.5 – (a) Time domain waveforms, the red trace is displaced ~1/2 a period with respect to the black trace. (b) FFT of the fullwaveform. (c) FFT and spectral phase of a 1.6 μs segment of the waveform. A constant offset and a linear trend have been removed from the phase plot. Only the phase values where the FFT has significant power are shown. The inset plot shows the errors of the phase compared to the theoretically expected values.

The phase of the optical field changes periodically with time. The phase of the downconverted RF waveform is expected to change in the same way. There is an additional slowly varying phase factor that undergoes a random walk and it represents the phase between the local oscillator modes and the CW laser (ϕ_0). This can be observed when the signal is recorded for times longer than the inverse of the individual combline linewidth. The phase of the photodetected RF waveform will then have a time dependence given by

$$\phi(t) = \beta \sin\left(2\pi\Delta f_{rep} t + \phi_M\right) + \phi_0 \tag{8.1}$$

Interestingly, while the phase ϕ_0 undergoes a random walk, its *derivative* has zero mean, and therefore, the frequency modulation of the waveform is not affected by this term beyond a zero-mean random quantity. That is, $f(t) = \frac{1}{2\pi}\frac{d\phi}{dt} = \Delta f_{rep}\beta \cos\left(2\pi\Delta f_{rep} t + \phi_M\right) + \phi_0{}'$, and $\langle \phi_0{}' \rangle \sim 0$.

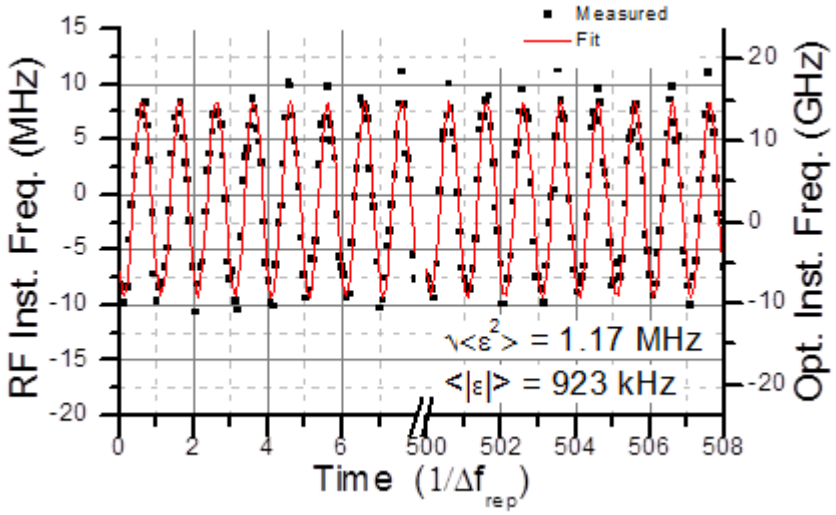

Figure 8.6 – Instantaneous frequency of the photodetected waveform. RF on the left y axis and optical in the right axis. Notice the compression between the two scales. The rms and mean absolute error are indicated in the figure. The fit errors are ~5% of the full range.

The recorded time domain data can be analyzed in several ways. For example, from the previous RF spectrum (and knowledge of the ratio of Bessel functions), the depth of phase modulation index can be estimated at ~1.4 rad. Another way of measuring such modulation index is through a time domain analysis of the instantaneous frequency of the measured waveform. Figure 8.6 shows the measured instantaneous frequency and a calculated sinewave at the phase modulation frequency of the RF waveform (equal to the repetition-rate detuning) where only the phase factor ϕ_M was fit to the data. Notice that the sinewave does not go out of step with the frequency modulation even after hundreds of periods (Figure 8.6 shows 510 periods or ~80 μs). This is due to the fact that the optical phase drops out of the frequency modulation calculation and thus, the random walk that the relative phase between both lasers undergoes does not affect the measurement. The repetition rate detuning between the waveforms gives the compression factor, which can be used to calculate the instantaneous optical frequency of the phase-modulated light, shown in the right *y*-axis of Figure 8.6.

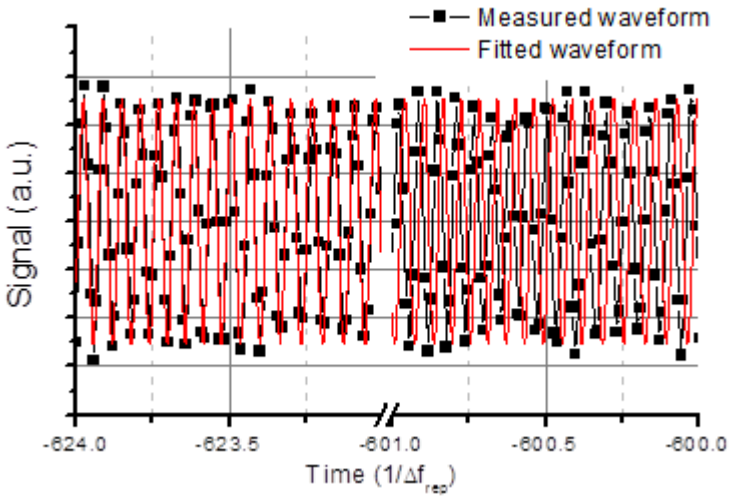

Figure 8.7 – Fitted time domain waveform. Notice that after a carrier frequency shift and bandwidth decompression, this corresponds exactly to the phase-modulated optical waveform.

The complete signal can be fit to a perfect phase-modulated waveform only for short time intervals, as the relative phase between the lasers undergo a random walk and, after several periods, the waveforms slowly go out of step. Figure 8.7 shows this effect, where a perfect phase-modulated sinewave was fit in a portion of the waveform and then followed several periods in time. After ~20 periods (~3.2 μs), the phase of the waveform is visibly changed. This is consistent with the linewidth of the local oscillator comblines, which is >100 kHz.

3.White light and periodically filtered white light

As a proof that the concept can be applied to a multi-heterodyne version of the experiment, a periodically filtered white light source was generated by taking Amplified Spontaneous Emission from a semiconductor optical amplifier and filtering it with a Fabry-Pérot etalon, followed by amplification stages to boost the power in each transmitted resonance. The FPE has 10.24 GHz of free-spectral range and a Finesse of ~100, making the width of each resonance of ~100 MHz. An actively, harmonically mode-locked laser where comb operation was forced by continuous-wave optical injection, such as the one described in [81], was used to down-convert this white light spectrum. The repetition rate detuning was adjusted to have a clear separation between resonances in the RF domain. The optical spectra of the sources are shown in Figure 8.8 (a), where a clear walk-off can be seen between the peaks. The photodetected signals were then interfered in the RF domain, generating a series of periodically spaced RF peaks, each with an interference pattern imposed upon it, as shown in Figure 8.8 (b) and (c).

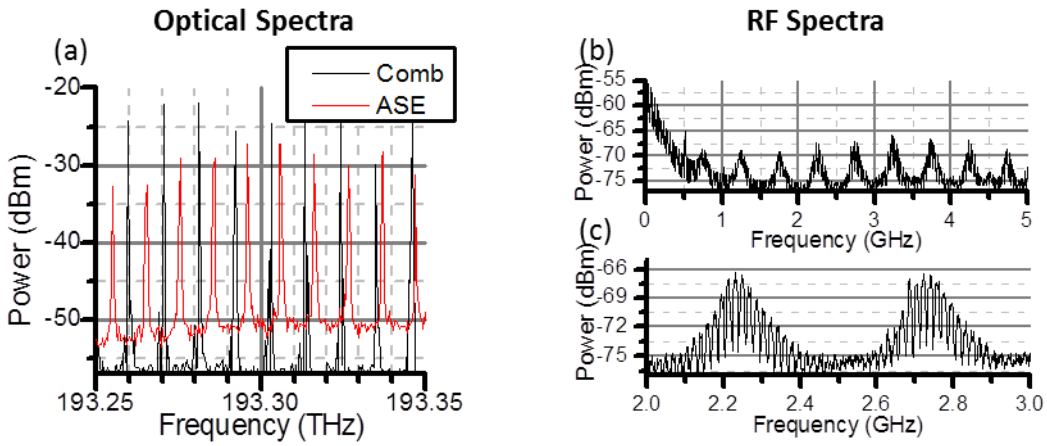

Figure 8.8 – Multiheterodyne white light interferometry. (a) Optical spectra of the periodically filtered white light (blue) and the mode-locked laser (red). (b) RF spectra of the interfering photocurrents of the downconverted white light.

An experiment was performed where the photocurrents were sampled independently and then interfered. The results are shown in Figure 8.9. A delay of ~12 m of fiber was added between the two arms and the waveforms sampled in two independent channels of a high-bandwidth oscilloscope. The sampled waveforms are shown in Figure 8.9 (b). It is interesting to note that while each of the waveforms is essentially noise (incoherent), the two waveforms are correlated with a delay of ~63 ns. The FFT spectra of these signals are shown in Figure 8.9 (c). When the signals are added, spectral interference can be observed in each of the down-converted ASE peaks. Figure 8.9 (d) shows the resulting interference. The transfer function of a spectral interferometer is shown in red for visual aid.

Since the interference pattern is sensitive to small path length deviations, another test was made where a single ASE peak and a continuous wave laser were used to measure the spectrogram of the interference while the optical path in one of the arms of the interferometer was driven by a piezo-electric fiber stretcher, as shown in Figure 8.10 (a). The spectrogram in Figure 8.10 (b) is obtained by calculating the interference pattern while a slow triangular modulation is imposed on

Δt_A. The function driving Δt_A is a 1 Hz triangular wave with a peak-to-peak amplitude of 4 fs. That is, the path delay between the two ASE paths is only changed by 4 fs (Δt_A = 20ns ± 2fs) or, close to a single cycle of a 200 THz carrier. The experimentally obtained spectrogram is shown in Figure 8.10 (c), where a clear periodic shift in the fringes is observed with a frequency of 1Hz.

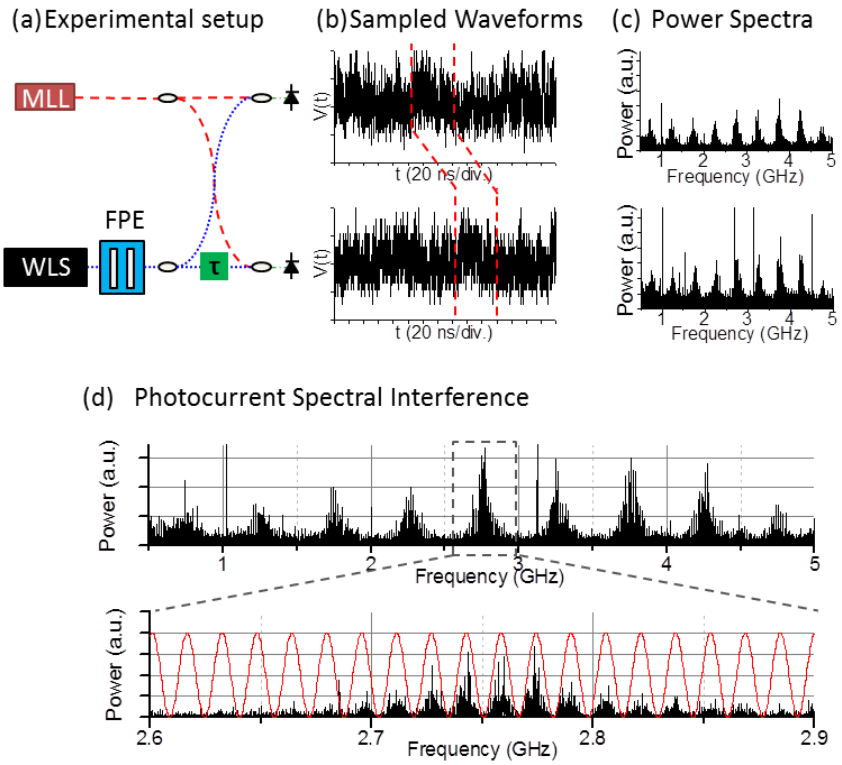

Figure 8.9 – Spectral interference of downconverted incoherent light. (a) Experimental setup. (b) Sampled RF waveforms. (c) Power spectra of the sampled waveforms. (d) Spectral interference with superposed transfer function of a spectral interferometer (red).

In conclusion, we have shown a series of experiments where the use of a comb source as a local oscillator to down-convert and compress optical signals is desirable. We have provided examples with coherent (too narrow-band to be observed in short observation times) sources where we have compressed the spectrum of phase modulated light waveforms by factors of ~1600x and mode-locked pulses by ~17,000x. The carrier frequencies were down-converted from the ~200

THz regime to the microwave regime ~100 MHz. An analysis is presented for white light heterodyne detection and interferometry. Interference patterns akin to those of spectral interferometry can be obtained in the microwave regime by adding the photocurrents. In this fashion, an extremely high-resolution version of white light spectral interferometry can be performed.

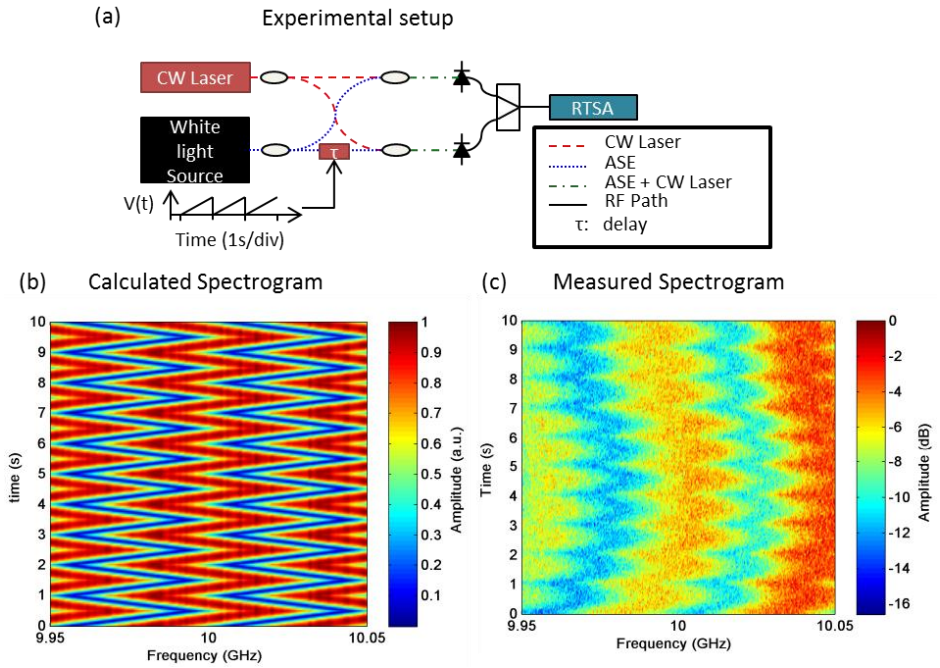

Figure 8.10 – Heterodyne photocurrent interferometry. (a) Experimental setup. (b) Calculated interferometry spectrogram. (c) Measured interferogram.

REFERENCES

1. J. Ye and S. T. Cundiff, *Femtosecond Optical Frequency Comb: Principle, Operation, and Applications* (Springer Verlag, 2005).

2. D. J. Jones, S. A. Diddams, J. K. Ranka, A. Stentz, R. S. Windeler, J. L. Hall, and S. T. Cundiff, "Carrier-Envelope Phase Control of Femtosecond Mode-Locked Lasers and Direct Optical Frequency Synthesis," Science **288**, 635–639 (2000).

3. R. Holzwarth, T. Udem, T. Hänsch, J. Knight, W. Wadsworth, and P. Russell, "Optical Frequency Synthesizer for Precision Spectroscopy," Physical Review Letters **85**, 2264–2267 (2000).

4. S. Diddams, D. Jones, J. Ye, S. Cundiff, J. Hall, J. Ranka, R. Windeler, R. Holzwarth, T. Udem, and T. Hansch, "Direct link between microwave and optical frequencies with a 300 THz femtosecond laser comb," Physical review letters **84**, 5102–5 (2000).

5. T. Rosenband, D. B. Hume, P. O. Schmidt, C. W. Chou, A. Brusch, L. Lorini, W. H. Oskay, R. E. Drullinger, T. M. Fortier, J. E. Stalnaker, S. A. Diddams, W. C. Swann, N. R. Newbury, W. M. Itano, D. J. Wineland, and J. C. Bergquist, "Frequency ratio of Al+ and Hg+ single-ion optical clocks; metrology at the 17th decimal place.," Science (New York, N.Y.) **319**, 1808–12 (2008).

6. C. Parthey, A. Matveev, J. Alnis, B. Bernhardt, A. Beyer, R. Holzwarth, A. Maistrou, R. Pohl, K. Predehl, T. Udem, T. Wilken, N. Kolachevsky, M. Abgrall, D. Rovera, C. Salomon, P. Laurent, and T. Hänsch, "Improved Measurement of the Hydrogen 1S–2S Transition Frequency," Physical Review Letters **107**, 1–5 (2011).

7. P. Gill, "Optical clocks coming of age," Nature **407**, 579–80 (2000).

8. T. Udem, S. Diddams, K. Vogel, C. Oates, E. Curtis, W. Lee, W. Itano, R. Drullinger, J. Bergquist, and L. Hollberg, "Absolute Frequency Measurements of the Hg+ and Ca Optical Clock Transitions with a Femtosecond Laser," Physical Review Letters **86**, 4996–4999 (2001).

9. T. W. Neely, T. A. Johnson, and S. A. Diddams, "High-power broadband laser source tunable from 30 μm to 44 μmbased on a femtosecond Yb:fiber oscillator," Optics Letters **36**, 4020 (2011).

10. F. Adler, P. Masłowski, A. Foltynowicz, K. C. Cossel, T. C. Briles, I. Hartl, and J. Ye, "Mid-infrared Fourier transform spectroscopy with a broadband frequency comb," Optics Express **18**, 21861 (2010).

11. A. Schliesser, M. Brehm, F. Keilmann, and D. W. van der Weide, "Frequency-comb infrared spectrometer for rapid, remote chemical sensing," Optics Express **13**, 9029 (2005).

12. A. Schliesser, N. Picqué, and T. W. Hänsch, "Mid-infrared frequency combs," Nature Photonics **6**, 440–449 (2012).

13. C. Gohle, T. Udem, M. Herrmann, J. Rauschenberger, R. Holzwarth, H. a Schuessler, F. Krausz, and T. W. Hänsch, "A frequency comb in the extreme ultraviolet.," Nature **436**, 234–7 (2005).

14. D. Z. Kandula, C. Gohle, T. J. Pinkert, W. Ubachs, and K. S. E. Eikema, "XUV frequency comb metrology on the ground state of helium," 18 (2011).

15. T. K. Allison, A. Cingöz, D. C. Yost, and J. Ye, "Extreme Nonlinear Optics in a Femtosecond Enhancement Cavity," America 1–10 (2011).

16. M. Fischer, N. Kolachevsky, M. Zimmermann, R. Holzwarth, T. Udem, T. W. Hänsch, M. Haas, U. D. Jentschura, and C. H. Keitel, "New Limits on the Drift of Fundamental Constants from Laboratory Measurements," Physical Review Letters **92**, 1–4 (2004).

17. T. Steinmetz, T. Wilken, C. Araujo-Hauck, R. Holzwarth, T. W. Hänsch, L. Pasquini, A. Manescau, S. D'Odorico, M. T. Murphy, T. Kentischer, W. Schmidt, and T. Udem, "Laser frequency combs for astronomical observations.," Science (New York, N.Y.) **321**, 1335–7 (2008).

18. D. A. Braje, M. S. Kirchner, S. Osterman, T. Fortier, and S. A. Diddams, "Astronomical spectrograph calibration with broad-spectrum frequency combs," The European Physical Journal D **48**, 57–66 (2008).

19. G. Walker, "Extrasolar planets: with a coarse-tooth comb.," Nature **452**, 538–9 (2008).

20. I. Coddington, W. C. Swann, L. Nenadovic, and N. R. Newbury, "Rapid and precise absolute distance measurements at long range," Nature Photonics **3**, 351–356 (2009).

21. S.-W. Kim, "Metrology: Combs rule," Nature Photonics **3**, 313–314 (2009).

22. S. Schiller, "Spectrometry with frequency combs," Optics letters **27**, 766–8 (2002).

23. I. Coddington, W. Swann, and N. Newbury, "Coherent Multiheterodyne Spectroscopy Using Stabilized Optical Frequency Combs," Physical Review Letters **100**, (2008).

24. N. R. Newbury, I. Coddington, and W. Swann, "Sensitivity of coherent dual-comb spectroscopy.," Optics express **18**, 7929–45 (2010).

25. B. Bernhardt, A. Ozawa, P. Jacquet, M. Jacquey, Y. Kobayashi, N. Picque, T. Udem, R. Holzwarth, G. Guelachvili, and T. W. Ha, "Cavity-enhanced dual-comb spectroscopy," **4**, 2009–2011 (2010).

26. T. Ideguchi, A. Poisson, G. Guelachvili, N. Picqué, and W. Theodor, "Adaptive real-time dual-comb spectroscopy," Sciences-New York 1–6 (n.d.).

27. P. J. Delfyett, S. Gee, H. Izadpanah, S. Ozharar, F. Quinlan, and T. Yilmaz, "Optical frequency combs from semiconductor lasers and applications in ultrawideband signal processing and communications," Journal of Lightwave Technology **24**, 2701–2719 (2006).

28. P. J. Delfyett, I. Ozdur, N. Hoghooghi, M. Akbulut, J. Davila-Rodriguez, and S. Bhooplapur, "Advanced Ultrafast Technologies Based on Optical Frequency Combs," IEEE Journal of Selected Topics in Quantum Electronics 1–17 (2011).

29. A. M. Weiner, "Femtosecond pulse shaping using spatial light modulators," Review of Scientific Instruments **71**, 1929 (2000).

30. G. C. Valley, "Photonic analog-to-digital converters.," Optics express **15**, 1955–82 (2007).

31. H. Taylor, "An optical analog-to-digital converter--Design and analysis," IEEE Journal of Quantum Electronics **15**, 210–216 (1979).

32. T. M. Fortier, M. S. Kirchner, F. Quinlan, J. Taylor, J. C. Bergquist, T. Rosenband, N. Lemke, a. Ludlow, Y. Jiang, C. W. Oates, and S. a. Diddams, "Generation of ultrastable microwaves via optical frequency division," Nature Photonics **5**, 425–429 (2011).

33. J. Millo, R. Boudot, M. Lours, P. Y. Bourgeois, A. N. Luiten, Y. Le Coq, Y. Kersalé, and G. Santarelli, "Ultra-low-noise microwave extraction from fiber-based optical frequency comb.," Optics letters **34**, 3707–9 (2009).

34. A. Haboucha, W. Zhang, T. Li, M. Lours, A. N. Luiten, Y. Le Coq, and G. Santarelli, "Optical-fiber pulse rate multiplier for ultralow phase-noise signal generation.," Optics letters **36**, 3654–6 (2011).

35. F. Quinlan, S. Ozharar, S. Gee, and P. J. Delfyett, "Harmonically mode-locked semiconductor-based lasers as high repetition rate ultralow noise pulse train and optical frequency comb sources," Journal of Optics A: Pure and Applied Optics **11**, 103001 (2009).

36. T. Yilmaz, C. M. Depriest, a. Braun, J. H. Abeles, and P. J. Delfyett, "Noise in fundamental and harmonic modelocked semiconductor lasers: Experiments and simulations," IEEE Journal of Quantum Electronics **39**, 838–849 (2003).

37. T. Yilmaz, C. Depriest, P. Delfyett, S. Etemad, a Braun, and J. Abeles, "Supermode suppression to below -130 dBc/Hz in a 10 GHz harmonically mode-locked external sigma cavity semiconductor laser.," Optics express **11**, 1090–5 (2003).

38. S. Gee, F. Quinlan, S. Ozharar, and P. J. Delfyett, "Correlation of supermode noise of harmonically mode-locked lasers," Journal of the Optical Society of America B **24**, 1490 (2007).

39. F. Rana, H. L. T. Lee, R. J. Ram, M. E. Grein, L. A. Jiang, E. P. Ippen, and H. A. Haus, "Characterization of the noise and correlations in harmonically mode-locked lasers," Journal of the Optical Society of America B **19**, 2609 (2002).

40. L. A. Jiang, E. P. Ippen, and H. Yokoyama, "Semiconductor mode-locked lasers as pulse sources for high bit rate data transmission," Journal of Optical and Fiber Communications Reports **2**, 1–31 (2005).

41. G. Roelkens, L. Liu, D. Liang, R. Jones, a. Fang, B. Koch, and J. Bowers, "III-V/silicon photonics for on-chip and intra-chip optical interconnects," Laser & Photonics Reviews **4**, 751–779 (2010).

42. S. R. Jain, M. N. Sysak, G. Kurczveil, and J. E. Bowers, "Integrated hybrid silicon DFB laser-EAM array using quantum well intermixing.," Optics express **19**, 13692–9 (2011).

43. S. Gee, F. Quinlan, S. Ozharar, and P. J. Delfyett, "Simultaneous optical comb frequency stabilization and super-mode noise suppression of harmonically mode-locked semiconductor ring laser using an intracavity etalon," IEEE Photonics Technology Letters **17**, 199–201 (2005).

44. E. Rubiola and V. Giordano, "Advanced interferometric phase and amplitude noise measurements," Review of Scientific Instruments **73**, 2445 (2002).

45. E. Rubiola, *Phase Noise and Frequency Stability in Oscillators* (Cambridge University Press, 2009).

46. E. Rubiola, V. Giordano, and J. Groslambert, "Very high frequency and microwave interferometric phase and amplitude noise measurements," Review of Scientific Instruments **70**, 220–225 (1999).

47. E. Rubiola, E. Salik, S. Huang, N. Yu, and L. Maleki, "Photonic-delay technique for phase-noise measurement of microwave oscillators," Journal of the Optical Society of America B **22**, 987 (2005).

48. K. Volyanskiy, J. Cussey, H. Tavernier, P. Salzenstein, G. Sauvage, L. Larger, and E. Rubiola, "Applications of the optical fiber to the generation and measurement of low-

phase-noise microwave signals," Journal of the Optical Society of America B **25**, 2140 (2008).

49. F. Quinlan, S. Gee, S. Ozharar, and P. Delfyett, "The effects of filtering RF source phase noise by a low noise, high quality factor actively modelocked laser on the laser's absolute and relative phase noise," Optics Express **14**, 5346 (2006).

50. I. Ozdur, M. Akbulut, N. Hoghooghi, D. Mandridis, S. Ozharar, F. Quinlan, and P. J. Delfyett, "A Semiconductor-Based 10-GHz Optical Comb Source With Sub 3-fs Shot-Noise-Limited Timing Jitter and ~500-Hz Comb Linewidth," IEEE Photonics Technology Letters **22**, 431–433 (2010).

51. E. D. Black, "An introduction to Pound–Drever–Hall laser frequency stabilization," American Journal of Physics **69**, 79 (2001).

52. R. W. P. Drever, J. L. Hall, F. V. Kowalski, J. Hough, G. M. Ford, A. J. Munley, and H. Ward, "Laser phase and frequency stabilization using an optical resonator," Applied Physics B Photophysics and Laser Chemistry **31**, 97–105 (1983).

53. K. Sarwar Abedin, N. Onodera, and M. Hyodo, "Repetition-rate multiplication in actively mode-locked fiber lasers by higher-order FM mode locking using a high-finesse Fabry–Perot filter," Applied Physics Letters **73**, 1311 (1998).

54. K. S. Abedin, N. Onodera, and M. Hyodo, "Higher order FM mode locking for pulse-repetition-rate enhancement in actively mode-locked lasers: theory and experiment," IEEE Journal of Quantum Electronics **35**, 875–890 (1999).

55. E. Rubiola, M. Olivier, and J. Groslambert, "Phase noise in the regenerative frequency dividers," IEEE Transactions on Instrumentation and Measurement **41**, 353–360 (1992).

56. N. K. Fontaine, D. J. Geisler, R. P. Scott, T. He, J. P. Heritage, and S. J. B. Yoo, "Demonstration of high-fidelity dynamic optical arbitrary waveform generation.," Optics express **18**, 22988–95 (2010).

57. R. P. Scott, N. K. Fontaine, J. P. Heritage, and S. J. B. Yoo, "Dynamic optical arbitrary waveform generation and measurement.," Optics express **18**, 18655–70 (2010).

58. R. H. Walden, "Analog-to-digital converter survey and analysis," IEEE Journal on Selected Areas in Communications **17**, 539–550 (1999).

59. P. W. Juodawlkis, J. C. Twichell, G. E. Betts, J. J. Hargreaves, R. D. Younger, J. L. Wasserman, F. J. O'Donnell, K. G. Ray, and R. C. Williamson, "Optically sampled analog-to-digital converters," IEEE Transactions on Microwave Theory and Techniques **49**, 1840–1853 (2001).

60. T. M. Fortier, M. S. Kirchner, F. Quinlan, J. Taylor, J. C. Bergquist, T. Rosenband, N. Lemke, A. Ludlow, Y. Jiang, C. W. Oates, and S. A. Diddams, "Photonic Generation of Low-Phase-Noise Microwave Signals," Arxiv:1101.3616 1–17 (2011).

61. F. Quinlan, T. M. Fortier, M. S. Kirchner, J. A. Taylor, M. J. Thorpe, N. Lemke, A. D. Ludlow, Y. Jiang, and S. A. Diddams, "Ultralow phase noise microwave generation with an Er:fiber-based optical frequency divider," Optics Letters **36**, 3260 (2011).

62. J. Davila-Rodriguez, I. Ozdur, C. Williams, and P. J. Delfyett, "A semiconductor-based, frequency-stabilized mode-locked laser using a phase modulator and an intracavity etalon," Optics Letters **35**, 4130 (2010).

63. P. W. Juodawlkis, J. J. Plant, W. Loh, L. J. Missaggia, K. E. Jensen, and F. J. O'Donnell, "Packaged 1.5-μm Quantum-Well SOA With 0.8-W Output Power and 5.5-dB Noise Figure," IEEE Photonics Technology Letters **21**, 1208–1210 (2009).

64. W. Loh, J. J. Plant, J. Klamkin, J. P. Donnelly, F. J. O'Donnell, R. J. Ram, and P. W. Juodawlkis, "Noise Figure of Watt-Class Ultralow-Confinement Semiconductor Optical Amplifiers," IEEE Journal of Quantum Electronics **47**, 66–75 (2011).

65. S. Gee, F. Quinlan, S. Ozharar, P. J. Delfyett, J. J. Plant, and P. W. Juodawlkis, "Ultralow-noise mode-locked optical pulse trains from an external cavity laser based on a slab coupled optical waveguide amplifier (SCOWA)," Optics Letters **30**, 2742 (2005).

66. Z. Jiang, D. S. Seo, D. E. Leaird, and a M. Weiner, "Spectral line-by-line pulse shaping.," Optics letters **30**, 1557–9 (2005).

67. a. M. Zolot, F. R. Giorgetta, E. Baumann, J. W. Nicholson, W. C. Swann, I. Coddington, and N. R. Newbury, "Direct-comb molecular spectroscopy with accurate, resolved comb teeth over 43 THz," Optics Letters **37**, 638 (2012).

68. F. Quinlan, S. Gee, S. Ozharar, and P. J. Delfyett, "Ultralow-jitter and -amplitude-noise semiconductor-based actively mode-locked laser," Optics Letters **31**, 2870 (2006).

69. S. A. Diddams, L.-S. Ma, J. Ye, and J. L. Hall, "Broadband optical frequency comb generation with a phase-modulated parametric oscillator," Optics Letters **24**, 1747 (1999).

70. T. Udem, J. Reichert, R. Holzwarth, and T. W. Hänsch, "Accurate measurement of large optical frequency differences with a mode-locked laser," Optics Letters **24**, 881 (1999).

71. T. Udem, R. Holzwarth, and T. W. Hänsch, "Optical frequency metrology.," Nature **416**, 233–7 (2002).

72. M. Akbulut, S. Bhooplapur, I. Ozdur, J. Davila-Rodriguez, and P. J. Delfyett, "Dynamic line-by-line pulse shaping with GHz update rate.," Optics express **18**, 18284–91 (2010).

73. S. Bhooplapur, N. Hoghooghi, and P. J. Delfyett, "Pulse shapes reconfigured on a pulse-to-pulse time scale by using an array of injection-locked VCSELs.," Optics letters **36**, 1887–9 (2011).

74. I. Coddington, W. C. Swann, and N. R. Newbury, "Coherent linear optical sampling at 15 bits of resolution.," Optics letters **34**, 2153–5 (2009).

75. F. Ferdous, D. E. Leaird, C.-B. Huang, and A. M. Weiner, "Dual-comb electric-field cross-correlation technique for optical arbitrary waveform characterization.," Optics letters **34**, 3875–7 (2009).

76. F. R. Giorgetta, I. Coddington, E. Baumann, W. C. Swann, and N. R. Newbury, "Fast high-resolution spectroscopy of dynamic continuous-wave laser sources," Nature Photonics **4**, 853–857 (2010).

77. A. D. Ludlow, X. Huang, M. Notcutt, T. Zanon-Willette, S. M. Foreman, M. M. Boyd, S. Blatt, and J. Ye, "Compact, thermal-noise-limited optical cavity for diode laser stabilization at 1x10(-15).," Optics letters **32**, 641–3 (2007).

78. Y. Y. Jiang, A. D. Ludlow, N. D. Lemke, R. W. Fox, J. A. Sherman, L.-S. Ma, and C. W. Oates, "Making optical atomic clocks more stable with 10−16-level laser stabilization," Nature Photonics 3–6 (2011).

79. B. Young, F. Cruz, W. Itano, and J. Bergquist, "Visible Lasers with Subhertz Linewidths," Physical Review Letters **82**, 3799–3802 (1999).

80. R. Hanbury Brown and R. Q. Twiss, "Interferometry of the Intensity Fluctuations in Light. I. Basic Theory: The Correlation between Photons in Coherent Beams of Radiation," Proceedings of the Royal Society A: Mathematical, Physical and Engineering Sciences **242**, 300–324 (1957).

81. C. Williams, F. Quinlan, and P. J. Delfyett, "Injection-Locked Mode-Locked Laser With Long-Term Stabilization and High Power-per-Combline," IEEE Photonics Technology Letters **21**, 94–96 (2009).